JGR Oceans

RESEARCH ARTICLE
10.1029/2022JC019623

Key Points:

- The variability of bottom currents in the Drake Passage is described using the ocean reanalysis GLORYS12
- Bottom currents are strongly controlled by the topography and are often disconnected from the surface circulation
- Sedimentary processes are dominated by the influence of local topography and bottom currents

Correspondence to:
G. Kreps,
gaston.kreps@awi.de

Citation:
Kreps, G., Lembke-Jene, L., Romero, S., Ferrari, R., Lamy, F., & Miramontes, E. (2023). Bottom-current variability and the relationship with topography and sedimentary processes in the Drake Passage. *Journal of Geophysical Research: Oceans*, *128*, e2022JC019623. https://doi.org/10.1029/2022JC019623

Received 28 DEC 2022
Accepted 10 AUG 2023

Author Contributions:
Conceptualization: Gastón Kreps, Ramiro Ferrari
Data curation: Gastón Kreps, Lester Lembke-Jene
Formal analysis: Gastón Kreps, Elda Miramontes
Investigation: Gastón Kreps, Lester Lembke-Jene
Methodology: Gastón Kreps, Silvia Romero, Ramiro Ferrari
Project Administration: Lester Lembke-Jene, Silvia Romero, Frank Lamy
Resources: Frank Lamy
Software: Gastón Kreps
Supervision: Frank Lamy, Elda Miramontes
Validation: Silvia Romero, Ramiro Ferrari
Visualization: Elda Miramontes

Bottom-Current Variability and the Relationship With Topography and Sedimentary Processes in the Drake Passage

Gastón Kreps[1,2], Lester Lembke-Jene[1], Silvia Romero[2,3,4], Ramiro Ferrari[5], Frank Lamy[1], and Elda Miramontes[6,7]

[1]Alfred-Wegener-Institut Helmholtz-Zentrum für Meeres - und Polarforschung, Bremerhaven, Germany, [2]Departamento de Ciencias de la Atmósfera y de los Océanos, Facultad de Ciencias Exactas y Naturales, Universidad de Buenos Aires, Buenos Aires, Argentina, [3]Departamento Oceanografía, Servicio de Hidrografía Naval, Buenos Aires, Argentina, [4]Universidad de la Defensa Nacional (UNDEF), Buenos Aires, Argentina, [5]NOVELTIS, Labège, France, [6]Faculty of Geosciences, University of Bremen, Bremen, Germany, [7]MARUM - Center for Marine Environmental Sciences, University of Bremen, Bremen, Germany

Abstract Bottom-current related sediments have been commonly used for paleoceanographic reconstructions. However, the strength and variability of bottom currents are poorly understood and thus the processes that control sedimentation in deep environments are not clear. In this study, we focus on the Drake Passage, which is connected to the Antarctic Circumpolar Current, that has a major impact on the global climate. We studied the intensity and variability of bottom currents and how they are related to sedimentary processes. For this purpose, we used 27-years from GLORYS12 Mercator Ocean reanalysis at high resolution to evaluate the bottom current dynamics. Geophysical data and surface grain size measurements were used to identify the type of sediment deposits. Our results show that the dynamics of bottom currents is disconnected from the sea surface dynamics, and bottom circulation is strongly controlled by the rough topography of the Drake Passage. The patterns for the first modes of bottom-current variability are related to the local topography and seem to generally control the distribution of contourites. The second and third EOF modes show patterns in the bottom currents that differ from the mean field, and they may affect the rate of erosion and deposition differently. Time series of bottom currents reveals multiple high-speed current events, but contourite drifts seem to accumulate preferentially in zones of slow and stable bottom currents. Our study highlights the potential of using ocean reanalysis to better constrain bottom currents in zones of scarce data and to plan future campaigns of direct measurements.

Plain Language Summary As a result of its unique geography, the Southern Ocean contains the largest ocean current in the world ocean, the Antarctic Circumpolar Current (ACC). The Drake Passage (DP) is the major geographic constriction for the ACC and exerts a strong control on the exchange of physical, chemical, and biological properties between the ocean basins. Yet, the bottom dynamics and the relation with sedimentary processes remain to be studied. We analyzed the currents flowing near the seafloor using a high resolution (1°/12°) reanalysis and compared the bottom dynamics with the characteristics of the seafloor sediments obtained using geophysical data sets and sediment cores. We found that the complex topography of the DP plays an essential role in bottom-current dynamics and that the circulation pattern near the seabed is often different from the sea surface circulation. The largest sediment deposits are located in the zones with weakest bottom current activity.

1. Introduction

The existence of the Southern Ocean (SO) is possible because of the actual configuration of the continents after the opening of the Drake Passage (DP) 50-34 million years ago (Eagles & Jokat, 2014). The low-pressure systems found in the latitudes of the SO generate winds from the west that build the strongest current in the world, the Antarctic Circumpolar Current (ACC), that isolates Antarctica from the warmer waters in subtropical areas. The SO and its complex dynamics play a fundamental role in the global system (e.g., Meredith et al., 2011; Rintoul & Sokolov, 2001). This is mainly because of the transport of heat, momentum, carbon and biochemical components (e.g., Khatiwala et al., 2009; Marshall & Speer, 2012), as well as the formation of different water masses that are major drivers of the meridional overturning circulation (MOC) (e.g., Jacobs, 2004; Orsi et al., 1999).

Writing – original draft: Gastón Kreps
Writing – review & editing: Silvia Romero, Elda Miramontes

The ACC consists of a number of circumpolar fronts, which correspond to water mass boundaries as well as deep-reaching jets of eastward flow (Orsi et al., 1995). Sokolov and Rintoul (2009) showed that these multiple jets are aligned along particular streamlines of sea surface height. Park et al. (2019) and Park and Durand (2019) has constructed a map of the ACC fronts in based on mean dynamic topography from satellite altimetry (Figure 1).

The seafloor topography in the SO (see Dorschel et al. (2022) for a detailed bathymetry from the SO) presents prominent ridge systems (choke points), such as the complex ones in the DP (see Bohoyo et al. (2019) for a detailed bathymetry from the DP), where the ACC is constricted to a narrow geographical region (~800 km) between the southern tip of South America and the northern tip of the Antarctic Peninsula (AP) (Figure 1). Klinck (1985) and Klinck and Hofmann (1986) showed that the rugged bottom topography in the DP plays a dominant role in the variability of the currents. The variations in topography can alter the current field through topographic steering (Pedlosky, 1987). Mesoscale eddies are likely generated by baroclinic instability of the mean flow, gaining their energy from the massive potential energy available in the mean circulation (Gill et al., 1974). The eddies dominate the oceanic kinetic energy (KE) and, through their effect on transport, play a major role in the general circulation (Venaille et al., 2011). Altimetry has shown that there is high eddy kinetic energy (EKE) along the path of the ACC, and that the geographical distribution of the mean jets and their variability are strongly influenced by local bottom topography (Barré et al., 2011; Chelton et al., 1990).

Sediment deposits formed mainly under the influence of bottom currents (i.e., currents related to oceanographic processes flowing near the seafloor) are classified as contourites (Rebesco & Camerlenghi, 2008; Rebesco et al., 2014). Local dynamics of bottom currents (i.e., horizontal eddies) and topographic features will also influence in the formation of the contourites (e.g., Miramontes et al., 2021; Wilkens et al., 2021). Several studies show the presence of contourites deposits in the DP and relationship with hydrographic characteristics such as water masses to underline bottom current paths (e.g., Lobo et al., 2021; López-Quirós et al., 2020; Maldonado et al., 2003, 2005; Pérez et al., 2015). The relation between sediment and current dynamics can be addressed by the analysis of sediment grain size. The size of particles that are moved and deposited has been related to the speed of the responsible flow (e.g., Ledbetter & Johnson, 1976; McCave & Swift, 1976). The linear function between sortable silt means grain sizes ($\overline{SS}$, 10–63 μm) and bottom current velocities is typically applied for evaluating relative changes in the near-bottom velocities in deep-sea sediments (McCave et al., 1995; McCave & Hall, 2006). Under a given stress some grains and aggregates are deposited, while others of smaller settling velocity are kept in turbulent suspension and transported further down current (McCave et al., 2017). This proxy is controlled by selective deposition and removal of finer material by winnowing (McCave et al., 1995; McCave & Hall, 2006) and has been often used for paleoceanographic reconstructions, including to reconstruct the evolution of the ACC in the DP (e.g., Lamy et al., 2015; Toyos et al., 2020; Wu et al., 2021).

Despite the fact that the DP is the most well-known choke point from the ACC, the bottom dynamics and the relation with sedimentation is still poorly constrained, especially due to the paucity of direct measurements and the complex seafloor topography. General circulation reanalysis, that assimilate satellite altimetric and hydrographic data, provide dynamically consistent ocean state estimates (Artana et al., 2021a). They also allow to extend the information on bottom circulation in space and time and thus facilitate the comparison with seafloor morphology and sedimentation patterns (Miramontes et al., 2019). In this study, we aim to improve our understanding of the Antarctic Circumpolar Current dynamics in relation to the sedimentary processes that control seafloor morphology and surface sediment distribution in the Drake Passage. For this purpose, we use daily data (27 years) from the high-resolution (1°/12°) GLORYS12 reanalysis from Mercator Ocean, to study bottom current dynamics. Hydrographic, bathymetric, hydroacoustic, seismic data and sediment cores will complement the analysis. The paper is organized as follows: in Section 2 we describe the data and methods used, in Section 3 we present the results with focus in each sub region of the Drake Passage and in Section 4 we discuss the results and present perspectives.

2. Materials and Methods

2.1. GLORYS 12 Velocity Data

To compute the bottom velocities, we used the GLORYS12 reanalysis. GLORYS12 is a global eddy-resolving physical ocean and sea ice reanalysis at 1°/12° horizontal resolution covering the 1993-present altimetry period, designed and implemented in the framework of the Copernicus Marine Environment Monitoring Service

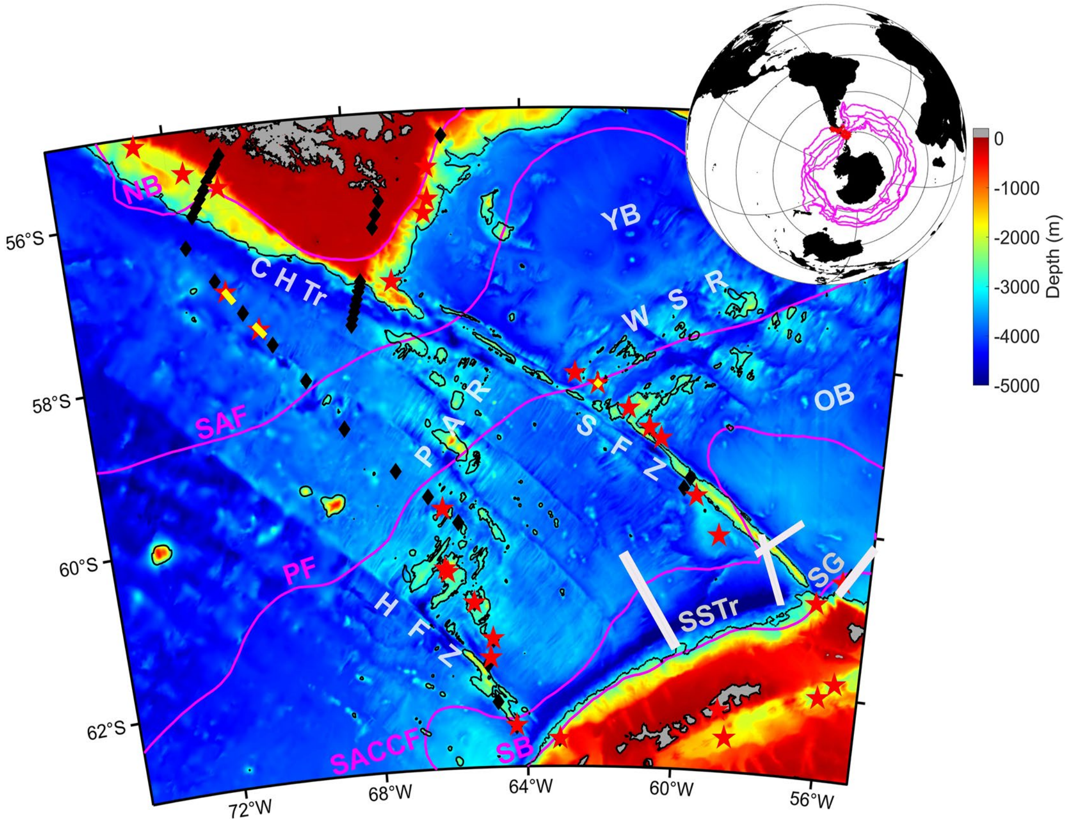

Figure 1. Drake Passage location and bathymetry derived from IBSCO v2. The location of CTD stations is represented with black diamonds and sediment cores with red stars, all collected during cruise PS97. The fronts from the Antarctic Circumpolar Current derived from satellite altimetry (Park et al., 2019) and Park and Durand (2019) are represented in purple solid lines. From North to South: NB = North Boundary, SAF = Sub Antarctic Front, PF = Polar Front, SACCF = Southern Antarctic Circumpolar Current Front; SB = Southern Boundary. White solid lines indicate the location of seismic profiles. Yellow solid segments indicate the location of PARASOUND profiles. Major ridges or fracture zones are indicated: Shackleton Fracture zone (SFZ); Phoenix Antarctic Ridge (PAR); West Scotia Ridge (WSR); Hero Fracture Zone (HFZ); South Shetland Trench (SSTr); Shackleton Gap (SG); Chilean Trench (CHTr); Yaghan Basin (YB) and Ona Basin (OB). Depth contours are shown for the 3,000-m isobath.

(CMEMS) (http://marine.copernicus.eu/). Ocean reanalysis aims at providing the most accurate past state of the ocean in its four dimensions (Lellouche et al., 2018). GLORYS12 is based on the current real-time global forecasting CMEMS system PSY4V3 (Lellouche et al., 2018). The vertical grid has 50 levels with 22 levels in the upper 100 m, leading to a vertical resolution of 1 m in the upper levels and 450 m resolution for the deepest levels up to a maximum depth of 5,727 m. The reanalysis is performed with a numerical model which physical component is the Nucleus for European Modeling of the Ocean (NEMO) (Madec et al., 2008). The model assimilates observations using a reduced-order Kalman filter with a 3-D multivariate modal decomposition of the background error and a 7-day assimilation cycle (Lellouche et al., 2013). Along-track satellite altimetric data from CMEMS (Pujol et al., 2016), satellite sea surface temperature from NOAA, sea-ice concentration, and in situ temperature and salinity vertical profiles from the latest CORA in situ databases (Cabanes et al., 2013; Szekeley et al., 2016) are jointly assimilated. A 3D-VAR scheme provides an additional 3-D correction for the slowly evolving large-scale biases in temperature and salinity when enough observations are available (Lellouche et al., 2018). GLORYS 12 reanalysis has been shown to correctly reproduce hydrography and velocities in the Argentine Basin and the DP, as compared with current meter data in the water column and 50 m above the seafloor (Artana et al., 2018a, 2018b, 2021a, 2021b).

In this study, we extracted 14 levels from 50 available, that correspond to the depths from 902 to 4,833 m that have been chosen to cover the deepest locations in the DP. With a focus on the period since satellite altimetry measurements of sea level has provided reliable information on ocean eddies, a daily data set is used that spans from 1 January 1993 to 31 December 2019 (27 years eq. to 9,861 days). The longitude was considered from 75° W to 55 W (241 values); the latitude from 55° S to 63° S (97 values). With this data, we have built a 4-dimensional Data Cube of longitude, latitude, depth and time (241, 97, 14, 9,861). The procedure consists in computing all 14 levels together to extract the value at each time and from the closest grid to the bottom. We computed the mean speed and the mean direction of the bottom current velocity in m/s and the bottom eddy kinetic energy (EKE) in m^2/s^2. The statistical analysis used in this work is the Empirical Orthogonal Functions (EOF). The utility of EOF analysis is that a small number of patterns may explain most of the variability in a data set. Furthermore, energetic events with different temporal structure should appear in different EOF modes, that is, patterns of variability can be separated (Klinck, 1985). For this purpose, the monthly mean bottom velocity was computed from daily data. The cut-off rule used to select the number of principal components (PC) to retain is the one proposed by Cattell (1966), known as the "scree test," which is based on plotting the eigenvalues as a function of the PC order number and looking for the break at which the eigenvalues become approximately constant. In our case we have selected the first 3 PC (eq. EOF). The data set was detrended and deseasoned and the EOF technic was performed following the method by Greene et al. (2019).

2.2. Hydrographic Survey (CTD)

The main instrumentation used was a SeaBird 911+ CTD (Conductivity, Temperature and Depth), with two temperature and conductivity sensors and additional oxygen, fluorescence and Beam Attenuation sensors (WET Labs), integrated in the water sampling rosette with 24 Niskin Bottles (Ocean Test Equipment Inc.) fired by an SBE32 carousel. The difference between both temperature and conductivity sensors was <0.003, °C and mS/cm, respectively. The GPS position at any time during the profile was added to the CTD bins by means of NMEA. The raw CTD data were processed with the SeaBird Data processing software according to SeaBird recommendations.

2.2.1. CTD Data Analysis

To determine which water masses are present in the CTD stations performed during cruise PS97, the neutral density (γ^n) (kg/m^3) was computed (Figure 1). Neutral density is a particularly useful parameter when tracing water masses that undergo extreme pressure changes. In contrast to the isopycnals approach based on matching various potential density surfaces with a discrete set of reference pressures, Jackett and MacDougall (1997) computed a neutral density variable that is locally referenced: a well-defined function that incorporates all nonlinear terms in the equation of state for seawater, including the one arising from the pressure dependency of the thermal expansion coefficient (Orsi et al., 1999). For intermediate and deep-water masses we use the definition of Antarctic Intermediate Water (AAIW) as $27.10 < \gamma^n < 27.60$ kg m^3, Upper Circumpolar Deep Water (UCDW) as $27.60 < \gamma^n < 27.90$ kg m^3, Middle Circumpolar Deep Water (MCDW) as $27.90 < \gamma^n < 28.10$ kg m^3, Lower Circumpolar Deep Water (LCDW) as $28.10 < \gamma^n < 28.27$ kg m^3 and Antarctic Bottom Water (AABW) as $\gamma^n > 28.27$ kg m^3 (Orsi et al., 1999; Valla et al., 2018; Well et al., 2003).

2.3. Geophysical Data Set (Multibeam Bathymetry, Sub-Bottom Profiler and Seismic Data)

Multibeam bathymetric data were recorded during cruise PS97 with the ATLAS Hydrographic HYDROSWEEP DS3 multibeam echo sounder permanently installed on the R/V Polarstern. The grid resolution we used in this work was 100 m. To cover most of the DP, we used the International Bathymetric Chart of the Southern Ocean Version 2 (IBSCO v2). IBCSO v2 is a regional mapping project of the General Bathymetric Chart of the Ocean (GEBCO). IBCSO v2 is a digital bathymetric model (DBM) for the area south of 50° S with special emphasis on the bathymetry of the Southern Ocean. IBCSO v2 has a resolution of 500 m × 500 m in a Polar Stereographic projection (EPSG: 9,354) (Dorschel et al., 2022).

The sediment echosounder PARASOUND DS III - P70 (Atlas Hydrographic, Bremen, Germany) is a sub-bottom profiler permanently installed aboard the R/V Polarstern. It records sea floor and sub-bottom reflection patterns and thus characterizes the upper sediment layers according to their acoustic behavior. The PARASOUND system makes use of the parametric effect to produce a secondary low frequency based on two primary high frequencies, allowing deeper penetration with high resolution (for details, see Grant & Schreiber, 1990). To enhance reflector coherency, the envelope was calculated and visualized with "The Kingdom Software" (IHS Markit).

The multichannel seismic reflection data used in this study were obtained from the Antarctic Seismic Data Library System for Cooperative Research and accessed through the GeoMapApp (http://www.geomapapp.org) and the Antarctic Seismic Data Library System (SDLS) (https://sdls.ogs.trieste.it) that is managed by the Istituto Nazionale di Oceanografia e Geofisica Sperimentale (OGS). The profiles used cover the southern part of the DP and were collected during the SA500, TH-88 and IT90AP cruises.

The SA500 cruise was carried out by Brazil in 1987–1988 using a source of 8 airguns (8.8 L), a 1,800 m long streamer with 72 channels and shot intervals of 50 m, with sampling rates of 4 ms. The TH-88 cruise was conducted in 1988–1989 by Japan. They used 2 water guns (13.1 L), a 600 m long streamer with 24 channels, the shot interval was 50 m and the sampling rate 4 ms. The ITP90AP cruise was performed by Italy in 1989 using an airgun array (2 × 18 guns) with a total volume of 45.56 L fired every 50 min with a sampling rate of 4 ms. The streamer was 2975 m long.

Sub-bottom profiler and seismic data were used to classify the types of sediments present in the DP and to identify the sediments affected by bottom currents (i.e., contourites). The identification of contourites is based on the morphology and internal architecture of the sediment bodies. We followed the concepts proposed by Faugères et al. (1999), Faugères and Stow (2008), Nielsen et al. (2008), and Rebesco et al. (2014), and used the classification and terminology proposed by Miramontes et al. (2021). The term "contourite drift" is used in this study to classify the main sediment accumulations formed by bottom currents, which commonly have a mounded shape. The term "moat" is used to refer to concave incisions that are located adjacent to contourite drifts and parallel to the slope of to a topographic obstacle. The moat is considered to host the core of a bottom current, and it can be used to interpret the direction of the bottom current along a slope because it forms when the Coriolis force forces the current toward the slope (Rebesco et al., 2014; and references therein). The location of contourites in the present study is based on our own interpretation and on previous studies in the region (Martos et al., 2013; Maldonado et al., 2014; López-Quirós et al., 2020.

2.4. Surface Sediments (Multicorer)

The multicorer permits the recovery of up to 12 surface sediment samples and the uppermost 30–60 cm of sediment, usually spanning the most recent geological history. A total of 51 seafloor surface samples were recovered in the DP region during R/V Polarstern Cruise PS97 in 2016 (Lamy, 2016). Samples were taken by a multicorer and, in a few cases, with a giant box Corer within a depth range of ~650–4,000 m water depth in order to obtain undisturbed surface samples of the uppermost centimeter of sediment. In our study, we used the grain size analyses of surface sediment samples (0–1 cm below the seafloor) carried out by Wu et al. (2019a, 2019b); in particular, the mean sortable silt, which is the mean size between 10 and 63 μm and is a proxy for paleoceanographic reconstructions (McCave et al., 1995). All data are available within the Pangaea data base (https://doi.org/10.1594/PANGAEA.907140).

3. Results

3.1. Hydrographic Features From Drake Passage

Results from 40 full-depth CTD stations collected during cruise PS97, allow us to track the presence of seven water masses due to their thermohaline properties (Figure 2). The range of potential temperature θ (°C) goes from close to −2°–10° (Figure 2a). The salinity range varies from 32.6 to 34.725 (Figure 2a). Four water masses are present at bottom layers in the study area (Figure 2). A clear division in the water masses of the upper layer, south and north of the Polar Front (PF) in agreement with Moore et al. (1999), Dong et al. (2006), and Barré et al. (2008), around latitude 59° S, which forms a boundary between Antarctic and sub-Antarctic water masses (Figures 2a and 2c). In contrast, this division is not found in the bottom layers (Figures 2a and 2c). Bottom layers show a clear isopycnal rise poleward, reaching surface layers close to the Antarctic continent (Figure 2c) (e.g., Deacon, 1937; Sverdrup, 1933; Speer et al., 2000; among others). In concordance with Naveira Garabato et al. (2002), we found that the Circumpolar Deep Water (CDW) is the most voluminous layer (Figure 2c). CDW is compound by UCDW, MCDW and the denser fraction is the LCDW. This last water mass is characterized by a salinity maximum (Figure 2) (e.g., Naveira Garabato et al., 2002). The older UCDW is lighter and presents an oxygen minimum in deep water masses (Figure 2b). The densest AABW presents an oxygen maximum and is fresher than the LCDW (Figure 2b). AABW was found only in the stations located east of the Shackleton Fracture Zone (SFZ) (Figures 2a and 2b), in concordance with Orsi et al. (1999). One of these stations is at the intersection of the SFZ and WSR and the other one, which has a lightly fresher signal (Figure 2b), is in the proximity of SG.

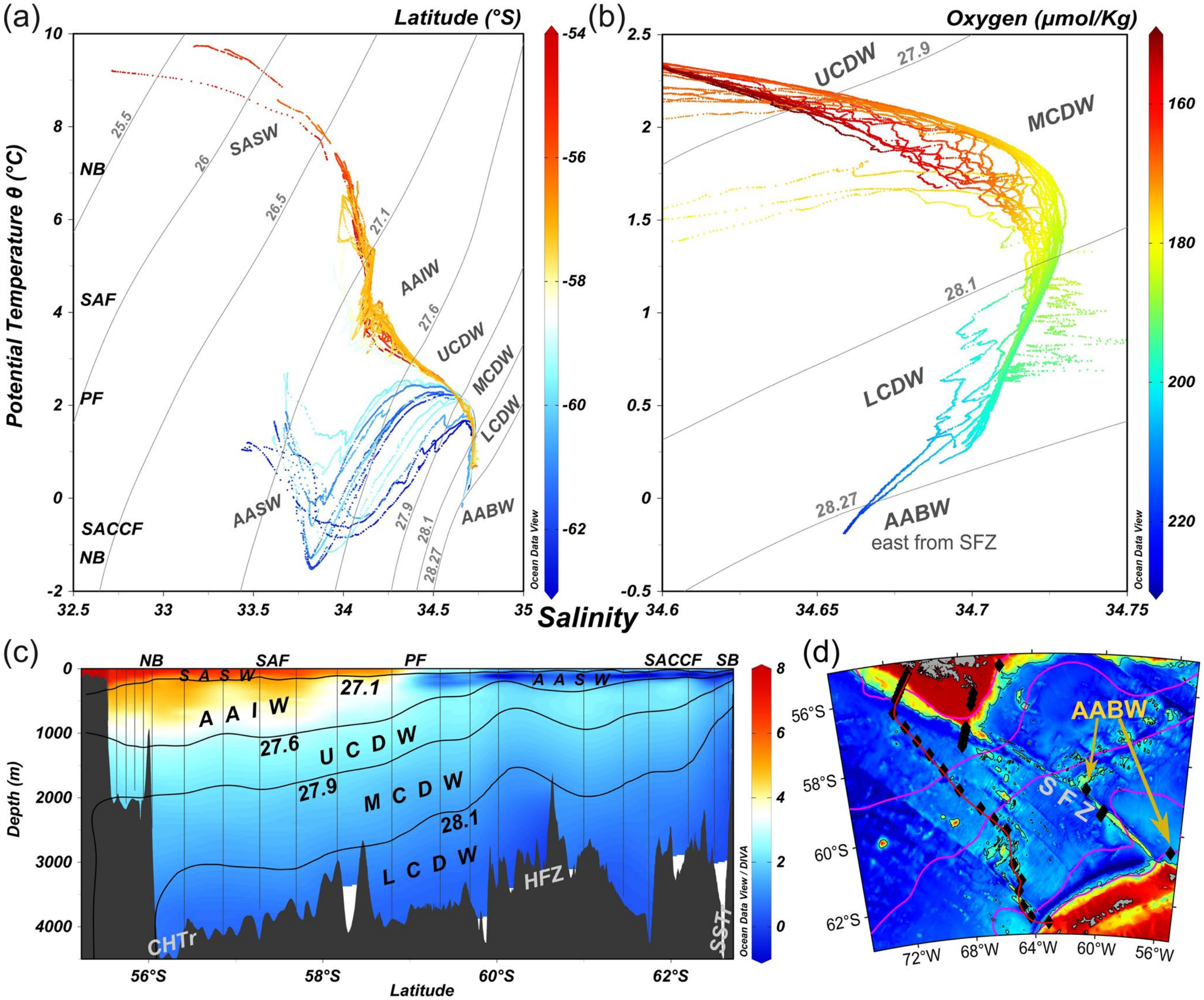

Figure 2. (a) Potential Temperature θ (°C)—Salinity plots, represent water masses in the Drake Passage (DP) obtained from CTD profiles measured during the PS97 cruise. Station locations are represented in (d). AABW = Antarctic Bottom Water; LCDW = Lower Circumpolar Deep Water; MCDW = Middle Circumpolar Deep Water; UCDW = Upper Circumpolar Deep Water; AAIW = Antarctic Intermediate Water; AASW = Antarctic Surface Water; SASW = Sub Antarctic Surface Water. Color bar represents latitudinal distribution of water masses. Gray solid lines indicate neutral density (γ^n) (kg/m^3) boundaries between different water masses. (b) Zoom to bottom layers, color bar represents oxygen (µmol/kg). (c) Hydrographic section across the West Drake Passage (red solid line in (d)). The color bar indicates potential temperature θ (°C). Isopycnals of neutral density (γ^n) (kg/m^3) are shown in solid black lines. Thin vertical black lines represent CTD station locations. Antarctic Circumpolar Current front mean locations are indicated on top, from North to South: NB = North Boundary, SAF = Sub Antarctic Front, PF = Polar Front, SACCF = Southern Antarctic Circumpolar Current Front; SB = Southern Boundary. Topographic features Hero Fracture Zone (HFZ); South Shetland Trench (SSTr) and Chilean Trench (CHTr). (d) Bathymetric map of the Drake Passage showing the location of the CTD stations and the cross section shown in (c).

The observations agree with the simulation of Solodoch et al. (2022) that showed, using a tracer global simulation model, that this AABW is mainly formed in the Weddell Sea and in Prydz Bay.

3.2. Bottom Dynamics

3.2.1. Drake Passage

As we specify in Section 2, 14 levels and 27 years (1 January 1993 to 31 December 2019) of data from the GLORYS 12 reanalysis were taken in consideration in the present study. Mean velocity distribution (Figure 3) ranges from close to 0 m/s to a maximum mean value from about 0.50 m/s located at longitude 66°35′W, latitude 57°25′S. The maximum value of the whole time series is about 1.25 m/s located at longitude 55°10W, latitude

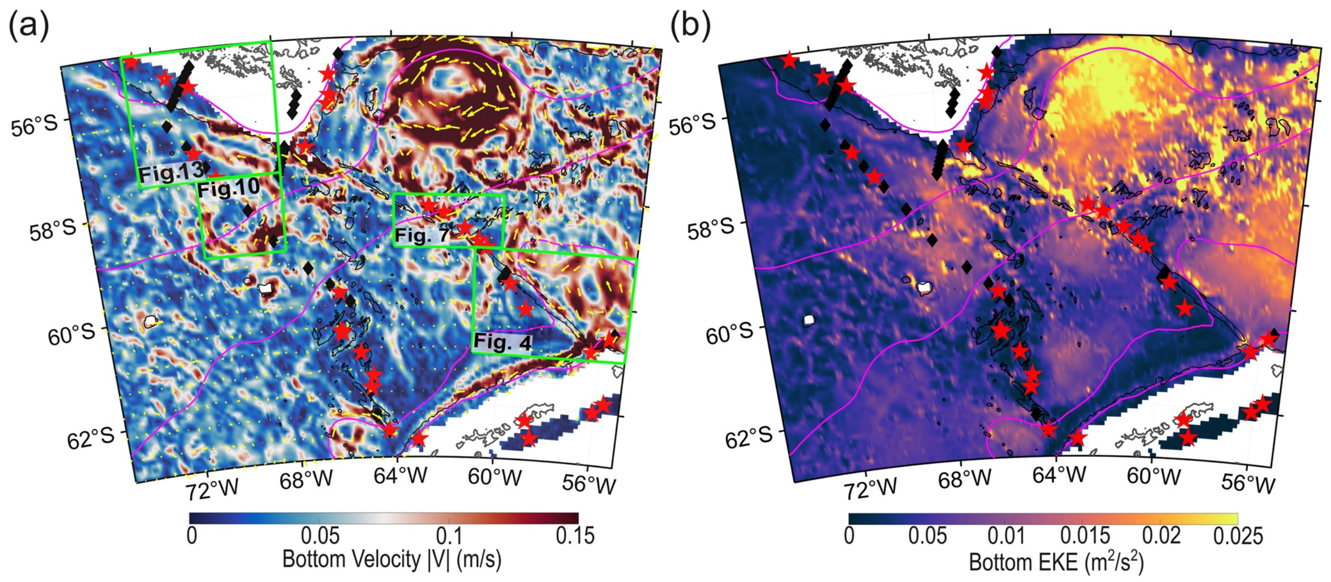

Figure 3. (a) Mean velocity (m/s) at bottom depth in the Drake Passage, calculated during 1993–2019 from reanalysis GLORYS12. The yellow arrows indicate the directions and intensities of mean currents. The mean locations of Antarctic Circumpolar Current front are indicated with purple solid lines. The locations of CTD stations are represented with black diamonds and sediment cores with red stars, all collected during cruise PS97. The green boxes represent the regions for analysis in this work. (b) Bottom eddy kinetic energy (EKE) (m^2/s^2) 1993–2019 from GLORYS12. Depth contours are shown for 3,000 m with black lines.

55°5′S and the date was 29 of July 2019. The reanalysis can resolve several gyres that are presented in these 27 years (Figure 3a). The main gyre is a cyclonic circulation in the YB, as was shown by Ferrari et al. (2012). Other small gyres are distributed in different locations in the DP (Figure 3a) and will be analyzed more in detail in the following sections. In addition, strong jets can be found at the bottom, as the one in the South Shetland Slope (SSS) and in the slope from the Chilean Trench (CHTr) (Figure 3a). The YB and Ona Basins (OB) are the most energetic regions from DP (Artana et al., 2021a; Ferrari et al., 2014), and present the highest bottom EKE values that reach up to 0.028 and 0.035 (m^2/s^2), respectively (Figure 3b).

For the purpose of this study, we separated the DP in different subregions (green boxes in Figure 3a) to make a more detailed analysis on the dynamics and sediment features.

3.2.2. Shackleton Fracture Zone—South

The first region to analyze is the Shackleton Fracture Zone South (SFZ_S). The SFZ is the main topographic feature in the DP through which the ACC has to pass over. It has a diagonal orientation from the tip of the TDFs to the confluence of the OB and the SSS in the south and constitutes the westernmost segment of the Scotia-Antarctic Plate boundary (Livermore et al., 2004). The mean velocity map shows a main jet that follow the SSS coming through the Shackleton Gap (SG) with strong bottom currents (Figure 4a). East from the SFZ, we observe a main stream in NW direction at the fracture slope. Eastwards of the SFZ, at the Ona Basin (OB), an anticyclonic recirculation is observed. This eastern region from the SFZ presented high values of EKE (Figure 4b). The region South West from the SFZ is dominated by low velocities and low EKE (Figures 4a and 4b).

In order to derive the leading modes of variability, an EOF analysis of bottom velocity was performed with 27 years of monthly detrended and deseasoned data. The first three modes of variability explain together 45% of the total variance (Figure 5). The first mode (28%) is related to local topography and could be considered as a monopole (Figure 5a). We extracted the day with the highest correlation (29 October 2010) from the time series associated with the first mode (Figure 5b). This day shows a similar pattern to the mean velocity of the whole period of study. The maximum velocity for this day was about 0.75 m/s located at longitude 57°25′W, latitude 59°55′S. But there is a difference east from the SFZ, the mean NW current is absent during this day (see Figures 3 and 4a). The second mode which represents 10% of the total variance presents a different pattern that could be considered as a dipole, between the jet in the SG and the SSS (South Shetland trench Slope) and the basins north of it (Figure 5c). Looking at the day with the highest correlation (05-Apr-2014), the strong gyre in the OB is absent (Figure 5d). In this case, the gyre located at the entrance of the SG is stronger and the flow into the SSS

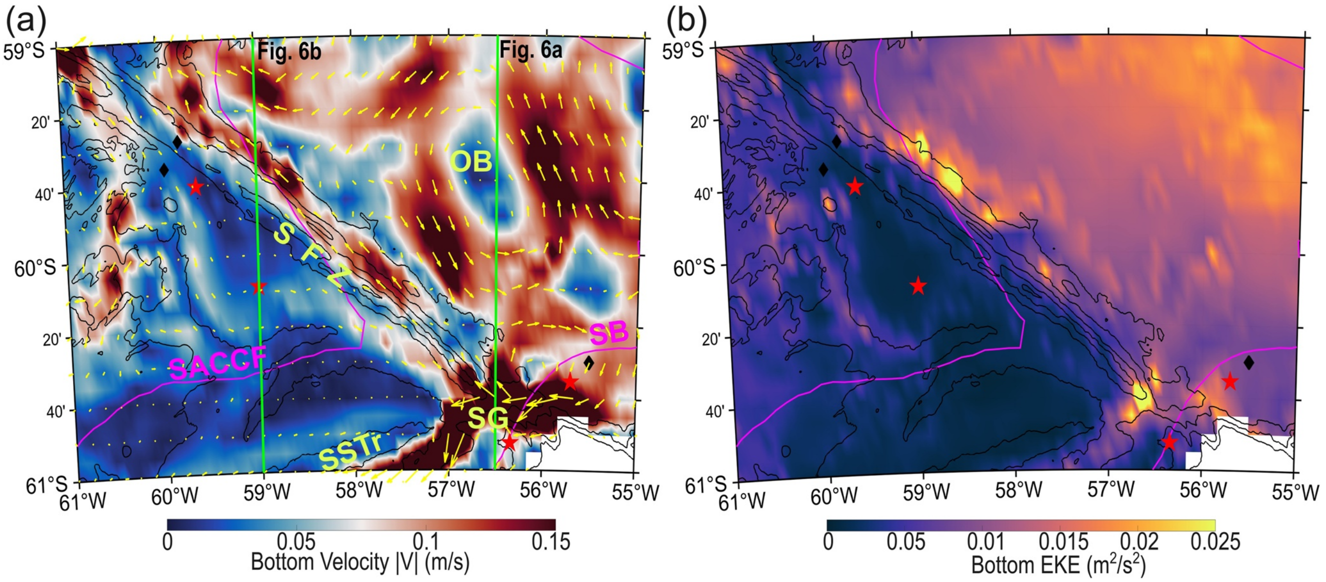

Figure 4. (a) Mean velocity (m/s) at bottom depth calculated during 1993–2019 from the GLORYS12 reanalysis at the southern region of the Shackleton fracture zone. The yellow arrows indicate the directions and intensities of mean currents. The mean locations of Antarctic Circumpolar Current front are indicated with purple solid lines, SACCF = Southern Antarctic Circumpolar Current Front and SB = Southern Boundary. (b) Bottom eddy kinetic energy (m^2/s^2) 1993–2019 from GLORYS12. Depth contours are shown with black lines every 1,000 m. The green meridian lines at longitude 59°W and 56.5°W indicate the position for the location of a time series (see Figure 6). The locations of CTD stations are represented with black diamonds and sediment cores with red stars, all collected during cruise PS97. Shackleton Fracture zone (SFZ); Shackleton Gap (SG); Chilean Trench (CHTr) and Ona Basin (OB).

is still present. The maximum velocity for this day was about 1.0 m/s located at longitude 55°50′W, latitude 60°40′S. The basin west from the SFZ is characterized by very low velocities (commonly below 0.22 m/s). The third mode, that represents 7% of the total variance, can be considered a dipole between east and west from the SFZ (Figure 5e). The day of the highest correlation (16 September 2011) shows a strong event in the basin west from the SFZ, that was not evident in the other modes or in the mean velocity field (Figure 5f). The maximum velocity for this day was about 0.79 m/s located at longitude 60°25′W, latitude 60°0′S. The flow close to the SFZ with SE direction continues and is added into the flow of the SSS. Another feature of this pattern is that no flow related to the Weddell Sea was coming from the OB. We observe that there is no flow going through the SG (Figure 5f).

To have a better comprehension of the dynamic of this region, a time series plot from the bottom velocity at a specific longitude location was extracted (Figure 6). As a way to understand the bottom flow and also the EOF analysis (Figure 5), this series shows the time variability of the bottom velocity during the whole period of analysis. At the fixed longitude of 56.5° W between latitudes 60.4° S and 60.8°S (Figure 6a), the presence of a jet can be detected in the SG (Figure 4a). This jet is not active at all times, it shows periods when the velocity is close to 0 m/s, for example, in 1999 and 2002 (Figure 6a white box). There are as well, periods when the jet shows a more intense flow at the bottom as the one between 2008 and 2011, and 2014 and 2015 (Figure 6a red box).

North from the jet the eddy is moving and occupying all the space within the basin, this can be seen by the elongated periods of strong velocities (Figure 6a red box). In Figure 6b, crossing the track at longitude 59° W, the presence of a NW flowing current in the eastern side of the SFZ (Figure 4a) can be observed. This flow shows events of more intense current (e.g., 2015 to 2016 red box Figure 6b) and events when it is slower (e.g., 2009 white box Figure 6b). In addition, the zone located west of the SFZ corresponds to a very low velocity region, which only presents some pulses of non-zero velocities at 60.4°S and 60.6°S that match with the mean location of the SACCF (Figures 4a and 6b).

3.2.3. Shackleton Fracture Zone—Center

The mean velocity (m/s) and direction from the Shackleton Fracture Zone Center (SFZ_C) observed in the bottom mean velocity field is dominated by the complex seafloor topography (Figure 7a). In the YB region, we observe a section from the anticyclonic gyre that has a location south of the main gyre of the YB as described

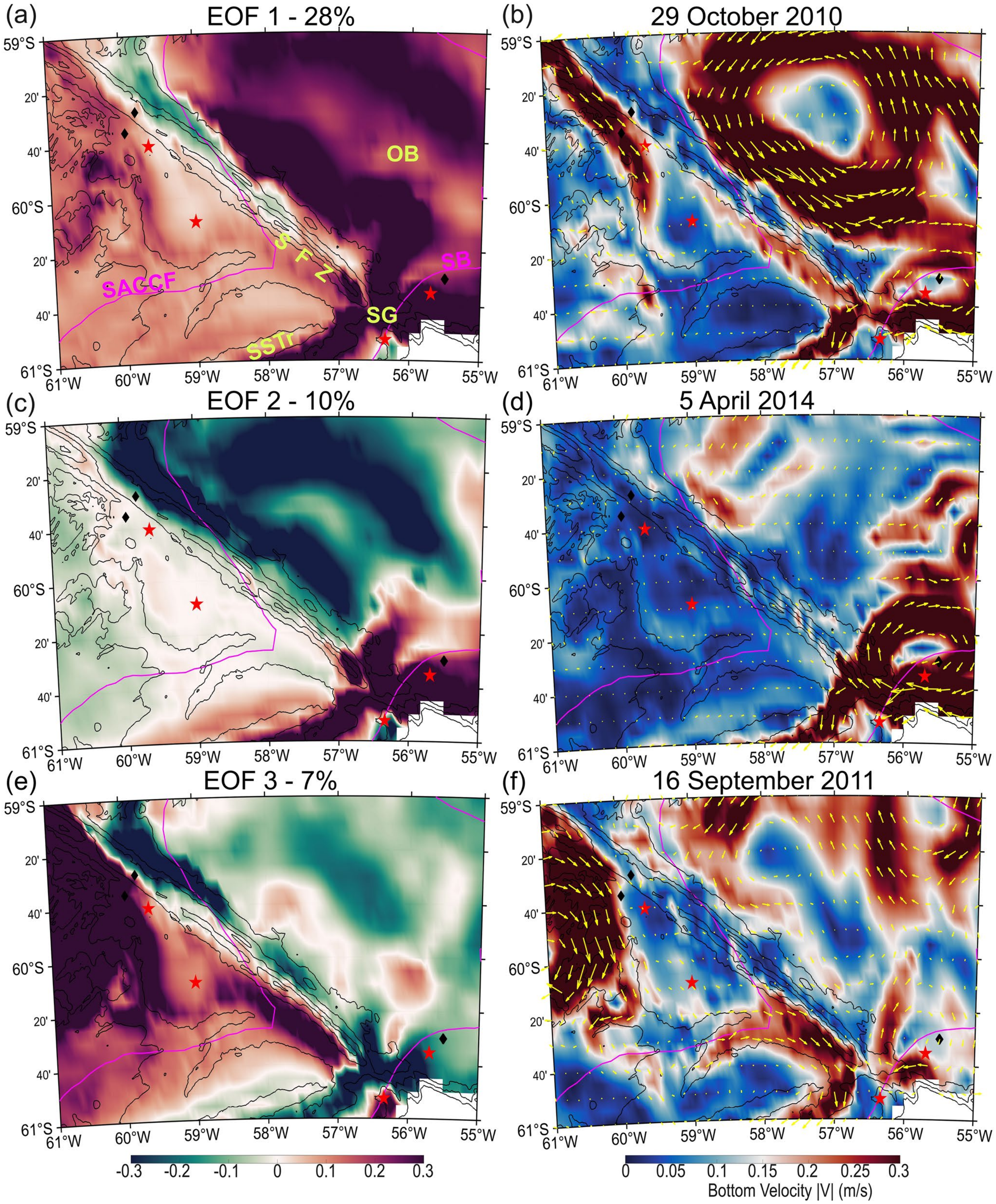

Figure 5. Empirical Orthogonal Function (EOF) analysis for the southern region of the Shackleton fracture zone (left panel). Days of the highest correlation with each mode for bottom velocity (m/s) (right panel). The mean locations of Antarctic Circumpolar Current front are indicated with purple solid lines, SACCF = Southern Antarctic Circumpolar Current Front and SB = Southern Boundary. Depth contours are shown with black lines every 1,000 m. Shackleton Fracture zone (SFZ); Shackleton Gap (SG); Chilean Trench (CHTr) and Ona Basin (OB).

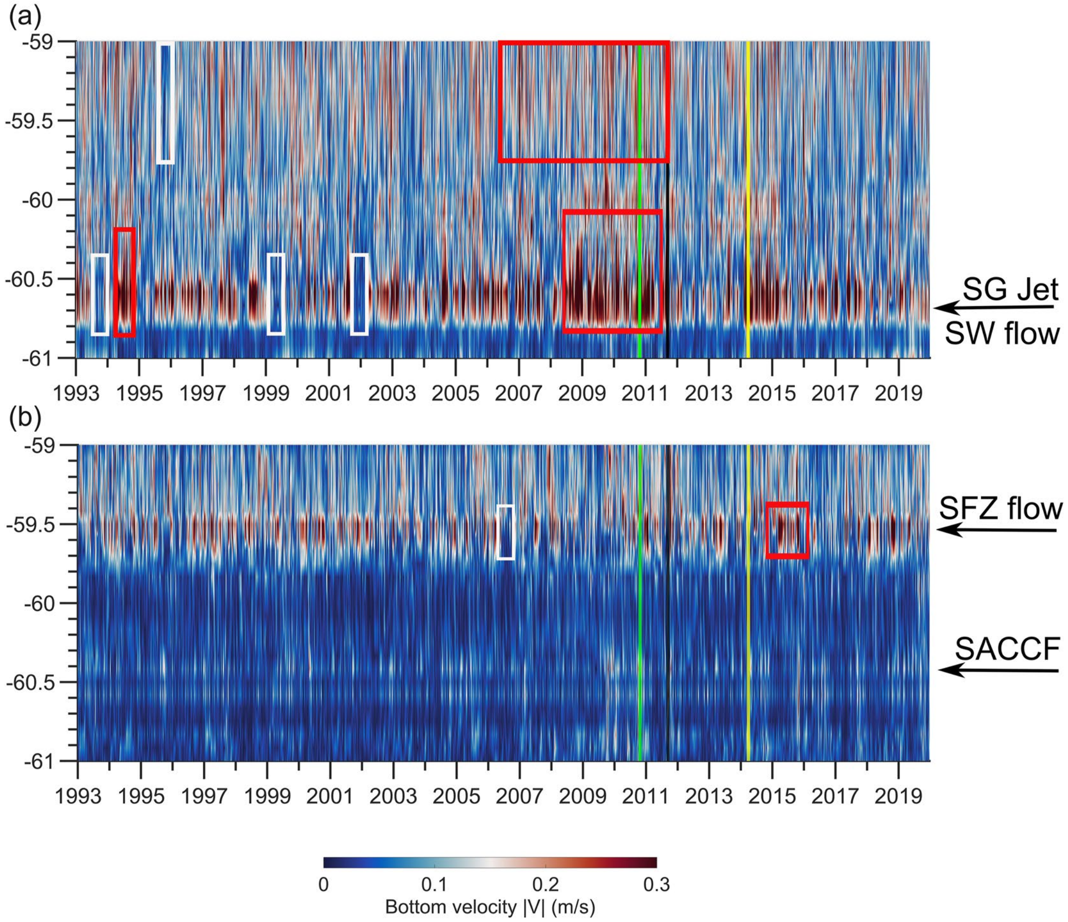

Figure 6. Time series (1 January 1993 to 31 December 2019, 27 years) of mean bottom velocity (m/s) along track at the southern region of the Shackleton fracture zone. (a) Longitude 56.5° W and at (b) longitude 59° W (see location in Figure 4a). Positions from flows, jets and fronts with black text and arrows. White boxes represent low velocities, red boxes represent high velocities events. The days with the highest correlations from EOF 1, 2 and 3 are shown as green, yellow and black lines, respectively.

before (Figure 3a). This gyre is limited by the SFZ and the WSR at each western and southern edges (Figure 7a). As it is reaches the WSR it matches the position of the PF and as it can be observed in Figure 3a, a train of gyres continues toward the east compressed by the main gyre of the YB the SAF and PF. South of the WSR, the velocity field shows less intensity (Figure 7a). The most energetic zones within this sub region are the YB and the area west from the SFZ (Figure 7b). South from the WSR, the EKE has lower values (Figure 7).

The EOF analysis from this sub region shows that the first three modes of variability explain together 47% of total variance (Figure 8). The first mode (Figure 8a) that presents a negative phase monopole dominated by the gyre within the YB. It shows that this region is separated from the one west of the SFZ and south of WSR. This first mode explains 21% of the total variance (Figure 8a). We extracted the day with the highest correlation (20 April 1997) from the time series associated with the first mode (Figure 8b). This day shows a similar pattern to the mean velocity of the whole period of study. A strong NW flow was found over the SFZ, which has no signal in the mean velocity field (see Figures 7a and 8b). The maximum velocity for this day was about 0.8 m/s located at longitude 63°15′W, latitude 58°20′S. The second mode explains 16% of the total variance (Figure 8c). This pattern shows a weak dipole limited by the PF and the SFZ (Figure 8c). The gyre from the YB is in negative phase and the region west from SFZ and south from the location of the PF is in positive phase. Looking at the region west from SFZ only, this pattern of negative phase (mode 1) and positive phase (mode 2) can be observed in both modes (Figures 8a and 8c). We extracted the day with the highest correlation (26 October 2019) from the time series associated with the second mode (Figure 8d). The flow that was in the NW direction on the day

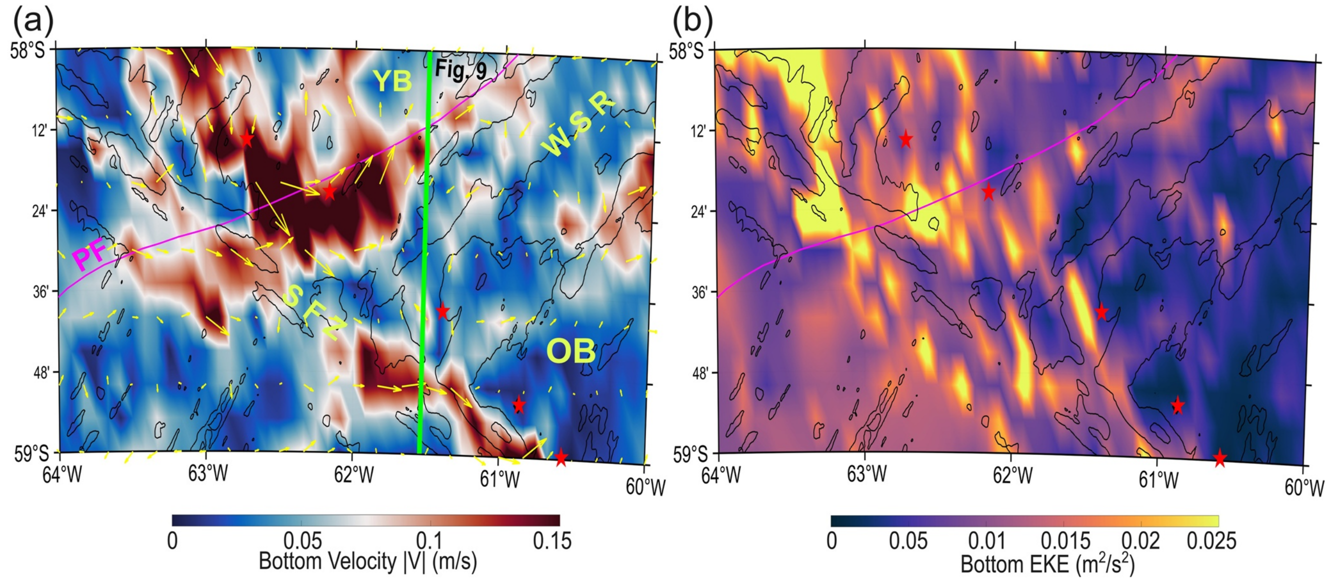

Figure 7. (a) Mean velocity (m/s) at bottom depth calculated during 1993–2019 from the GLORYS12 reanalysis at the center region of the Shackleton fracture zone. The yellow arrows indicate the direction and intensities of mean currents. The mean locations of Antarctic Circumpolar Current front are indicated with purple solid lines, PF = Polar Front. (b) Bottom eddy kinetic energy (EKE) (m^2/s^2) 1993–2019 from the GLORYS12 reanalysis. Depth contours are shown every 1,000 m with black lines. The green meridian line at longitude 61.5°W indicate the position for the location of a time series (see this figure). (c) The locations of CTD stations are represented with black diamonds and sediment cores with red stars, all collected during cruise PS97. Shackleton Fracture zone (SFZ); West Scotia Ridge (WSR); Yaghan Basin (YB) and Ona Basin (OB).

of the highest correlation for the first mode is in the SE direction over the SFZ in this second mode (Figures 8b and 8d). The maximum velocity for this day was about 0.68 m/s located at longitude 61°55′W, latitude 58°45′S. In both the first and second modes, there is flow at the same position of the PF. The third mode explains 10% of the total variance (Figure 8e). The pattern shows a dipole between the YB and the basin to the west of the SFZ and OB. While looking the day that has the highest correlation (2 March 2019), we can observe that the flow in the position of the PF is moved south (Figure 8d). The maximum velocity for this day was about 0.75 m/s located at longitude 63°15′W, latitude 58°25′S.

Figure 9 presents the time series extracted at longitude 61.5°W for the SFZ_C between latitudes 58°S and 59°S. Between 58.2°S and 58.3°S, the southern part of the gyre explained above (Figure 7a) can be observed, it matches the location of the PF at the surface. The edge of this gyre in the YB is not always active with events of quasi-zero velocities (m/s) in this region (e.g., 2004) (Figure 9 white box). This flow shows events of more intense current (e.g., 1993, 2008 red box Figure 9) It is interesting to note that there is a flow pattern south of 58.6°S that matches the possible initiation of a diffuse gyre west from SFZ, as we observe in Figure 3a, that is not completely resolved with this time series. This flow pattern, as shown in Figure 9, overpasses the SFZ and is split by a topographic feature. The region between 58.3°S and 58.5°S is dominated by slow velocities which can be explained by the presence of the WSR acting as a border.

3.2.4. West Drake Passage Zone—Center

Moving to the West from the SFZ, we name this zone as West Drake Passage Zone (WDPZ). This area is dominated by the Hero Fracture Zone in the south and the Phoenix Antarctic Ridge in the center, among other topographic features (Figure 1). This region can be considered as the entrance to the DP from the Pacific Ocean side.

The West Drake Passage Zone—Centre (WDPZ_C) mean velocity (m/s) field shows the presence of an anticyclonic gyre in these 27 years of data (Figure 10a). This bottom gyre is crossed by the SAF at the surface. A jet with a northwest direction can be observed coming out from the gyre (Figures 3a and 10a). South of the SAF, the mean velocity field is more intense than north of the SAF (Figure 10a). The center of the gyre is dominated mainly by low velocities and low EKE values (Figures 8a and 8b).

The first three modes of variability for the WDPZ_C explain together 47% of total variance (Figure 11). The first EOF mode shows a monopole in negative phase dominated by the structure of the gyre (Figure 11a). This

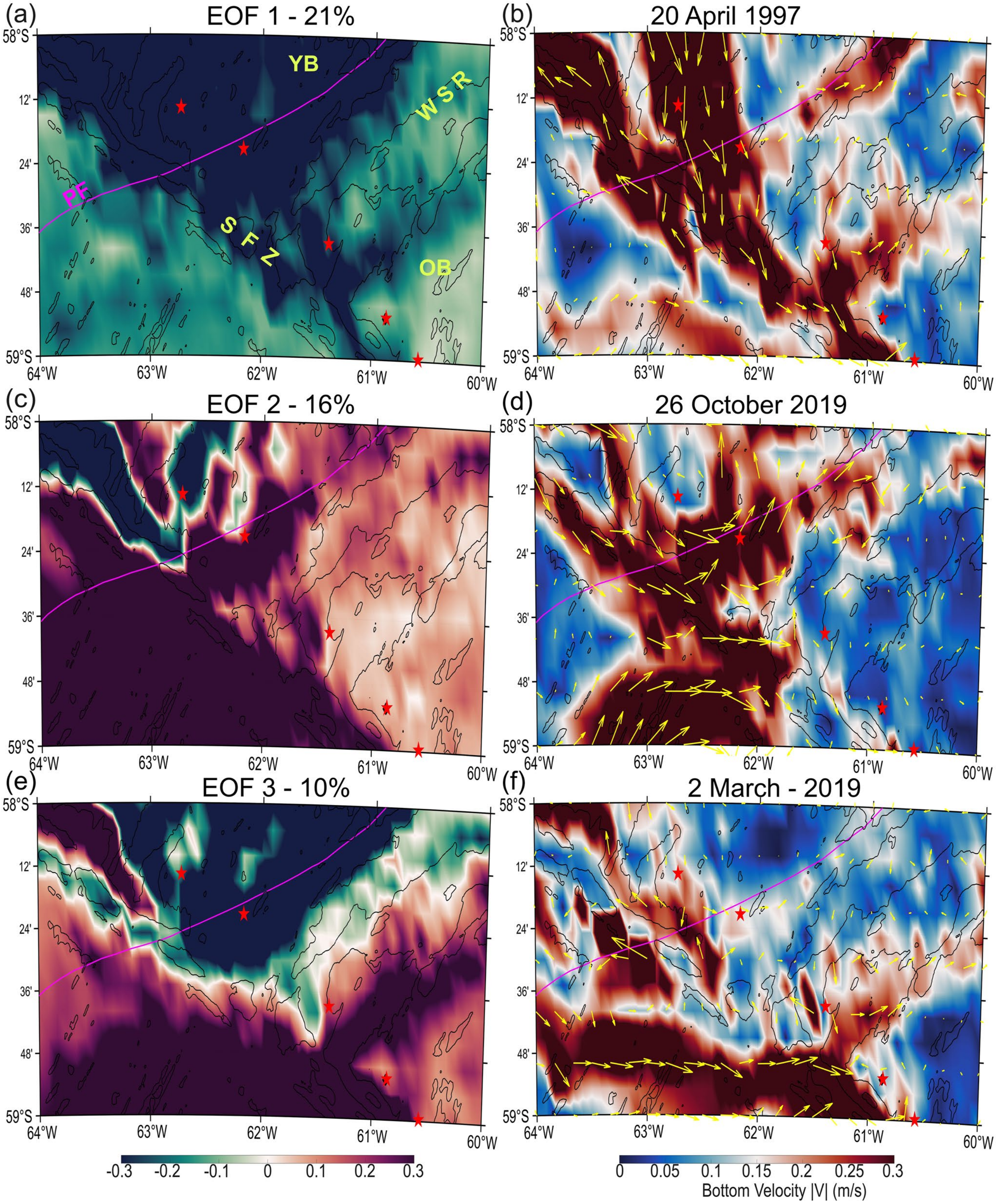

Figure 8. Empirical Orthogonal Function (EOF) analysis for the center region of the Shackleton fracture zone (left panel). Days of higher correlation with each mode for bottom velocity (m/s) (right panel). The mean locations of Antarctic Circumpolar Current front are indicated with purple solid lines, PF = Polar Front. Depth contours are shown every 1,000 m with black lines. Shackleton Fracture zone (SFZ); West Scotia Ridge (WSR); Yaghan Basin (YB) and Ona Basin (OB).

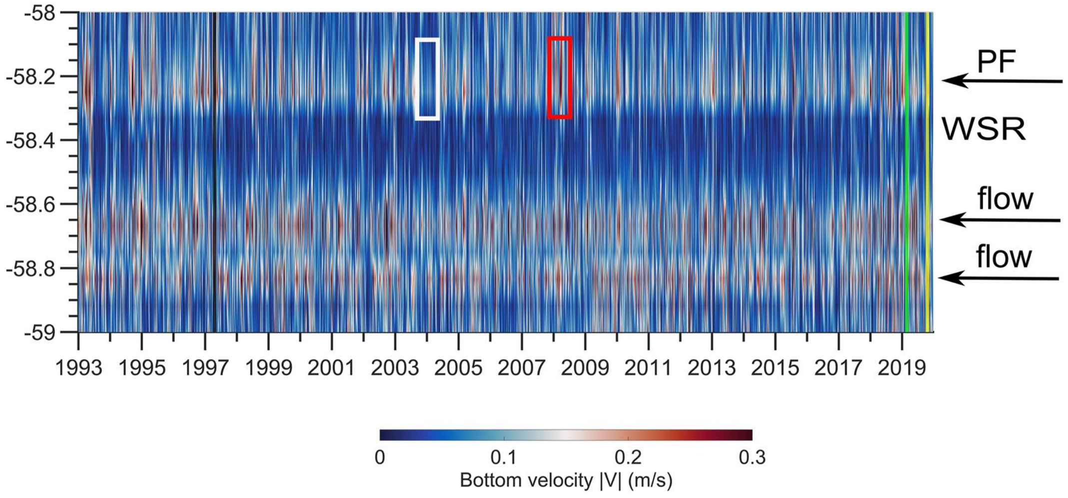

Figure 9. Time series (1 January 1993 to 31 December 2019, 27 years) of mean bottom velocity (m/s) along track for the center region of the Shackleton fracture zone. At longitude 61.5°W (see Figure 7a). Positions from flows and fronts with black text and arrows. White boxes represent low velocities, red boxes represent high velocities events. West Scotia ridge (WSR) locations with black text. The days with the highest correlations from EOF 1, 2 and 3 are shown as green, yellow and black lines, respectively.

mode explains 30% of the total variance. We extracted the day with the highest correlation (4 July 2014) from the time series associated with the first mode (Figure 8d). This day shows a similar pattern to the mean velocity (Figures 10a and 11b). The maximum velocity for this day was about 0.7 m/s located at longitude 70°35'W, latitude 58°45'S. The second mode explains 10% of the total variance and shows a dipole with a clear positive phase north of the position of the SAF and a negative phase south of the SAF (Figure 11c). The day with the highest correlation (3 December 2017) from the time series associated with the first mode (Figure 11d). The association

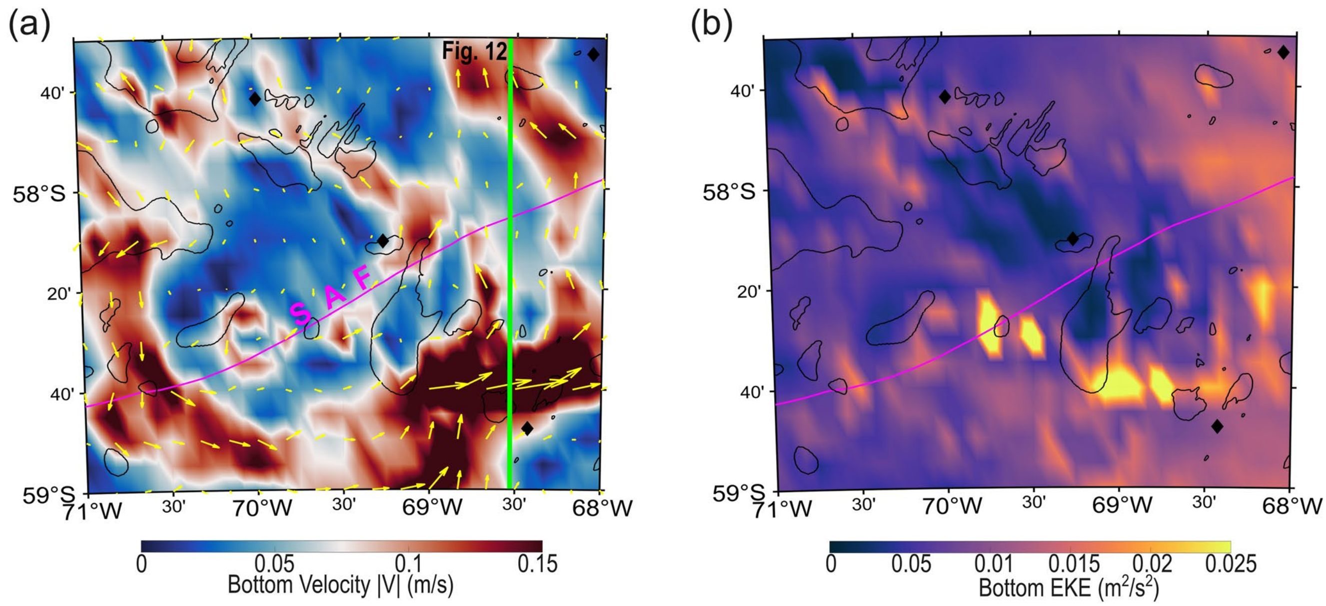

Figure 10. (a) Mean velocity (m/s) at bottom depth calculated during 1993–2019 from the GLORYS12 reanalysis at the center region of the West Drake Passage zone. The yellow arrows indicate the directions and intensities of mean currents. The mean locations of Antarctic Circumpolar Current front are indicated with purple solid lines, SAF = Sub Antarctic Front. The locations of CTD stations are represented with black diamonds and sediment cores with red stars, all collected during cruise PS97. (b) Bottom eddy kinetic energy (EKE) (m^2/s^2) 1993–2019 from the GLORYS12 reanalysis. Depth contours are shown every 1,000 m with black lines. The green meridian line at longitude 68.5°W indicate the position for the location of a time series (see Figure 9). The locations of CTD stations are represented with black diamonds and sediment cores with red stars, all collected during cruise PS97.

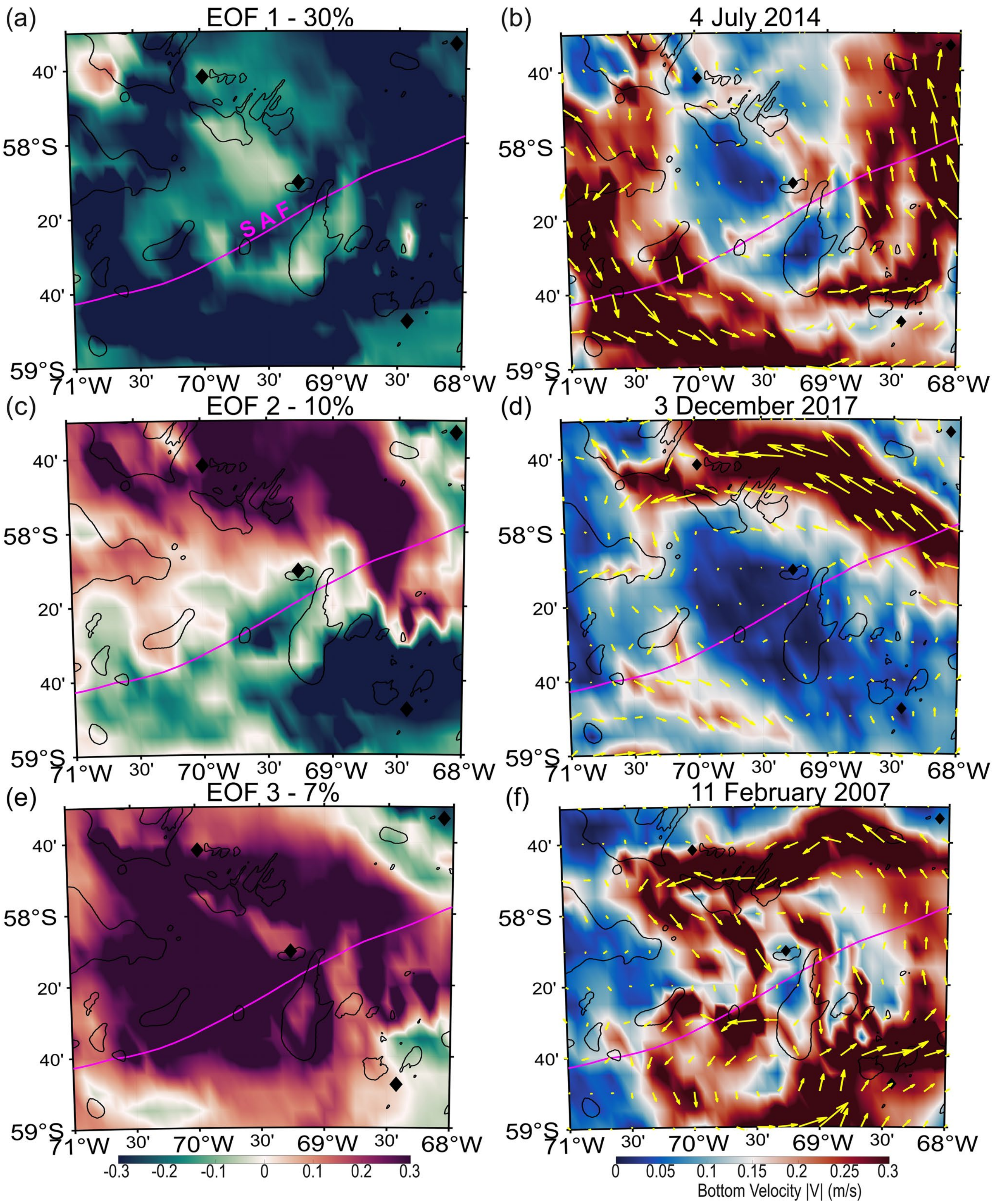

Figure 11. Empirical Orthogonal Function (EOF) analysis for the center region of the West Drake Passage zone (left panel). Days of the highest correlation with each mode for bottom velocity (m/s) (right panel). The mean locations of Antarctic Circumpolar Current front are indicated with purple solid lines, SAF = Sub Antarctic Front. Depth contours are shown every 1,000 m with black lines.

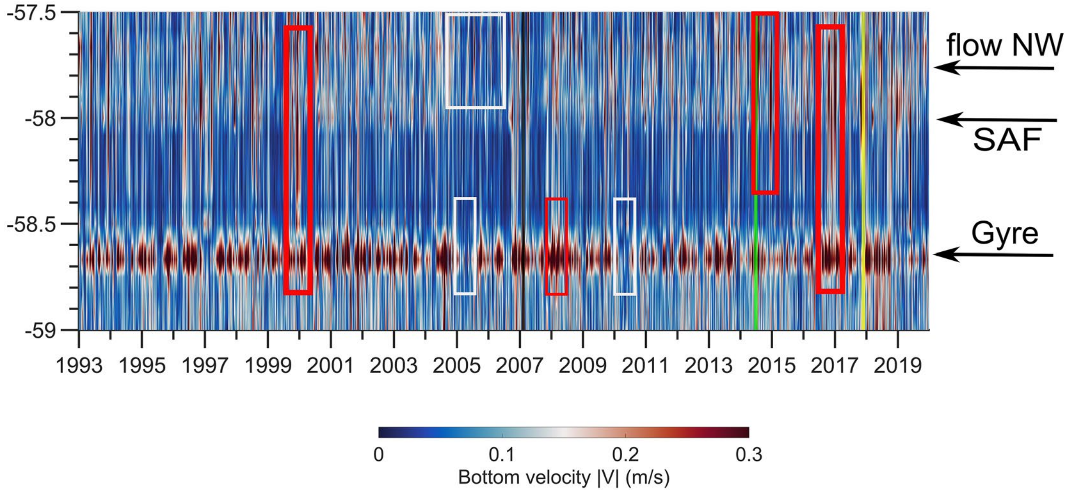

Figure 12. Time series (1 January 1993 to 31 December 2019, 27 years) of mean bottom velocity (m/s) along track for the center region of the West Drake Passage zone. At longitude 68.5°W (see Figure 8a). Positions from flows and fronts with black text and arrows. White boxes represent low velocities, red boxes represent high velocities events. The days with the highest correlations from EOF 1, 2 and 3 are shown as green, yellow and black lines, respectively.

with the second mode is a strong phase north of the SAF position and a low phase south of it for the bottom velocity (Figure 11d). The maximum velocity for this day was about 0.6 m/s located at longitude 69°5′W, latitude 56°40′S. The third mode explains 7% of the total variance (Figure 11e). This mode shows a strong monopole in the center of this area. While exploring the day with the highest correlation (11 February 2007) it shows that the gyre passes through the center of the region, where the mean velocity and the days associated with mode 1 and 2 are characterized by slow velocities (see Figures 10a and 11b, 11d, and 11f). Maximum bottom velocity of about 0.74 m/s located at longitude 69°0′W, latitude 59°0′S. Figure 12 shows the time series extracted at longitude 68.5°W where the gyre is strong and two prominent topographic features are present (one E and the other W from the 68.5°W meridian at 58°40′S Figure 10a). There is a clear pattern of strong bottom velocities at around 58.65°S that can be explained by the presence of the gyre (Figures 10a and 12). This pattern was not always present during the 27-year study period and there were events when the velocities dropped down to quasi zero m/s values (e.g., 2005, 2010 and 2019, white boxes in Figure 9). In contrast, this pattern was intensified in other events with velocities stronger than 0.3 m/s (Figure 12, red boxes). South of 58.7°S and up to 59°S, flow intensification can be observed that could be explained by gyre movements toward the east. For a particular time period, we can observe that there is a full intensification of the flow in this latitudinal gradient for, for example, end of 1999 and end of 2016 (Figure 12, red boxes). This is a clear pattern in the region between 58°S and 58.5°S, an area dominated by the SAF at the surface (Figure 10a). From 57.5°S to 58°S, a jet can be observed that goes out from the gyre in a northwest direction, with similar patterns of more and less intense fluctuations (Figures 10a and 12).

3.2.5. West Drake Passage Zone—North

Moving north from the WDPZ_C, we name this region as West Drake Passage Zone—North (WDPZ_N). The NB front from the ACC is following the bathymetry and a prominent jet with a southeast direction is observed with mean velocities stronger than 0.15 m/s (Figure 13a). In opposite direction, northwest, a jet is detected that goes out from the gyre in the WDPZ_C as mentioned above. This jet with a northwest direction seems to turn south after the overpass of topographic features and joins the gyre in WDPZ_C at its northwest corner (Figures 10a and 13a). The maximum values of EKE occur in the CHTr where these two jets are detected (Figure 13b). At the locations of the coring stations, shows a low value of EKE (Figure 13b).

The EOF analysis from this sub region shows that the first three modes of variability explain together 49% of total variance (Figure 14). The first mode of variability from the EOF analysis (Figure 14a) is a monopole with a negative phase in the CHTr and explains 30% of the total variance. The day with the highest correlation extracted from the time series of this first mode (01-Jun-2018) differs from the mean velocity pattern (Figures 13a and 14b). This day shows a strong NW flow over the CHTr. The maximum velocity for this day was about 0.62 m/s

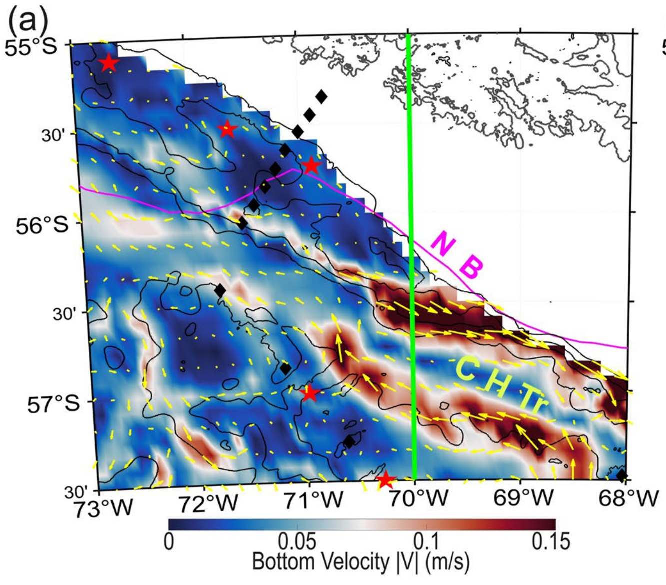

Figure 13. (a) Mean velocity (m/s) at bottom depth calculated during 1993–2019 from the GLORYS12 reanalysis at the northern region of the West Drake Passage zone. The yellow arrows indicate the directions and intensities of mean currents. The mean locations of Antarctic Circumpolar Current front are indicated with purple solid lines, NB = North Boundary. (b) Bottom eddy kinetic energy (EKE) (m^2/s^2) 1993–2019 from the GLORYS12 reanalysis. Depth contours are shown every 1,000 m with black lines. The green meridian line at longitude 70°W indicate the position for the location of a time series (see Figure 15). Note that no results are show at water depths above 900 m. The locations of CTD stations are represented with black diamonds and sediment cores with red stars, all collected during cruise PS97. Chilean Trench (CHTr).

located at longitude 72°0′W, latitude 56°0′S. The second mode of variability explains 12% of the total variance (Figure 14c). It presents a dipole with a strong positive phase with northwest and southeast flows and negative phase in between them in the CHTr. We extracted the day with the highest correlation (01-Dec-2017) from the time series associated with the first mode (Figure 14d). The velocity field for this day shows a SE flow in the N slope of the CHTr and a less intense opposite flow S of the CHTr. The maximum velocity for this day was about 0.64 m/s located at longitude 69°5′W, latitude 56°40′S. The third mode, that represents 7% of the total variance, can be considered a dipole between different sections CHTr with the slopes N and S of it (Figure 14e). The day with the highest correlation extracted from the time series associated with the third mode (23 November 2001) shows a strong current over the CHTr (Figure 14f). The maximum velocity for this day was about 0.51 m/s located at longitude 70°0′W, latitude 56°45′S.

The longitude selected to show a time series in WDPZ_N is 70°W (Figure 15). The southeastward flow, with the core at latitude 56.5°S, presents a pattern with disruptions (Figure 15 see white and red boxes). Between 2004 and 2010 a low phase of this particular flow can be observed. The northwest direction flow is located around latitude 57°S. The velocity pattern is not so strong as the one in the flow above and presets continues sequence of interruptions. The CHTr can be distinguish by a pattern of high and low velocities around latitude 56.75°S (Figure 15).

3.3. Current-Related Sedimentation

The largest contourite drifts in the study area have been identified in the southern region of the SFZ (Figure 16). In this area, contourite drifts are located on both sides of the fracture zone and are separated from the ridge by a moat. The contourite drifts are characterized on the multibeam bathymetry by the presence of a relatively smooth seafloor compared to the areas with less sediment accumulation, for instance in the central SFZ (Figures 16a and 17b). Based on the bathymetric data, the moat that is located west of the southern SFZ is around 4–6 km wide and about 200–300 m deep. It indicates the presence of a bottom current flowing toward the southeast along the fracture zone (Figures 16a, 16c, and 16d). The main contourite drift located east of the SFZ is located about 10–20 km east of the fracture zone and separated by a large irregular moat affected by local topographic highs. This moat indicates a main bottom current direction toward the northwest (Figures 16a and 16d). A similar moat

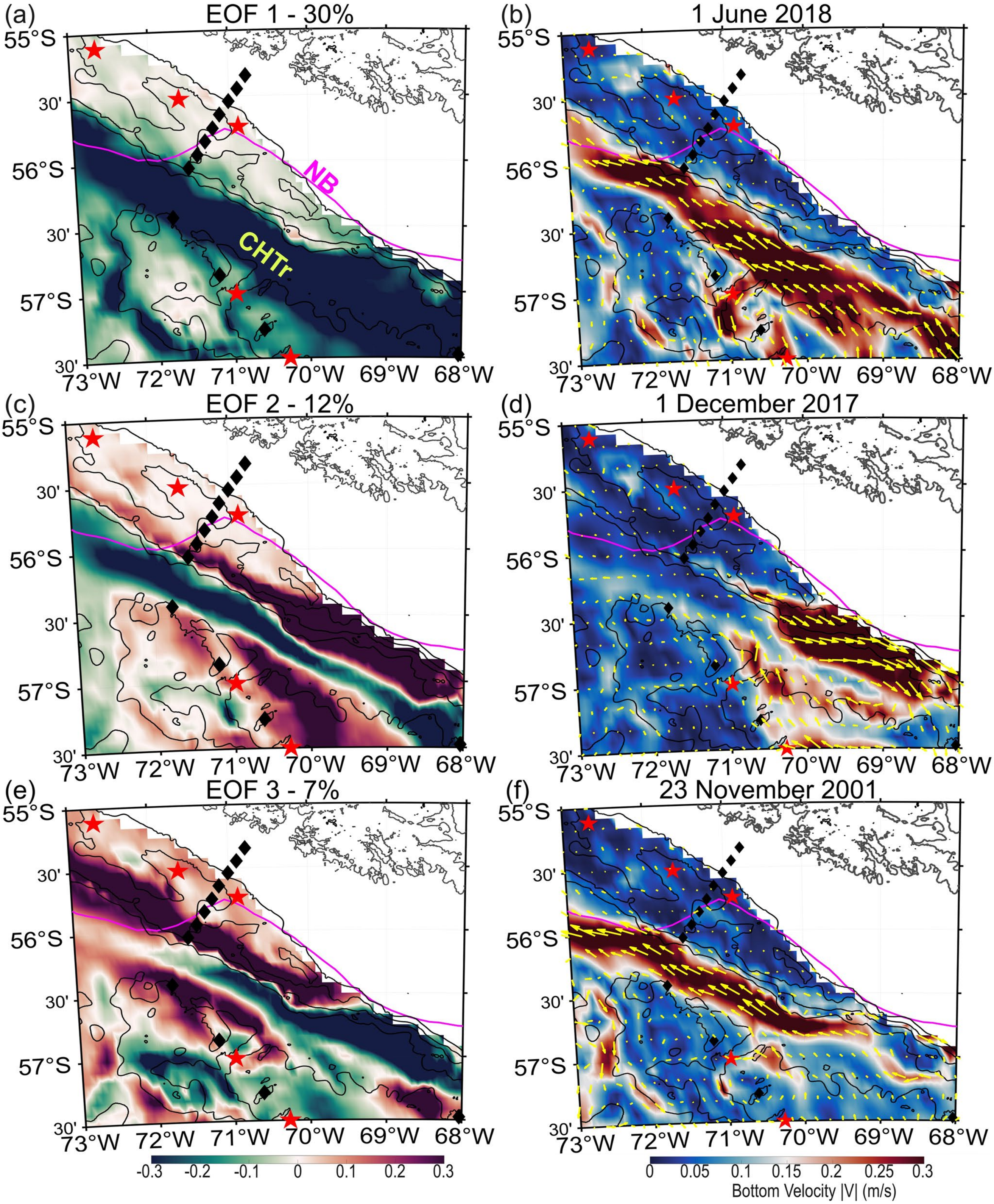

Figure 14. Empirical Orthogonal Function (EOF) analysis for the northern region of the West Drake Passage zone (left panel). Days of the highest correlation with each mode for bottom velocity (m/s) (right panel). The mean locations of Antarctic Circumpolar Current front are indicated with purple solid lines, NB = North Boundary. Depth contours are shown every 1,000 m with black lines. Chilean Trench (CHTr).

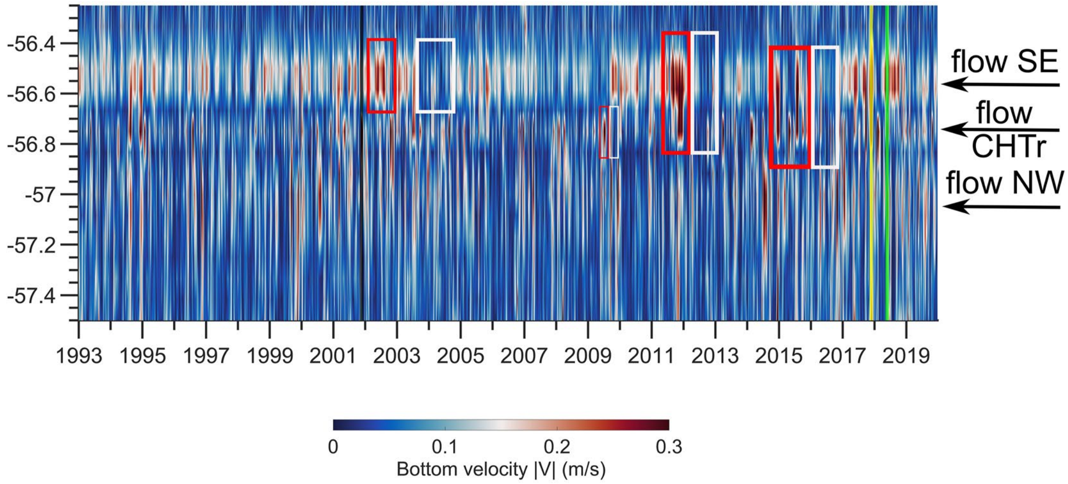

Figure 15. Time series (1 January 1993 to 31 December 2019, 27 years) of mean bottom velocity (m/s) along track for the northern region of the West Drake Passage zone. At longitude 70°W (see Figure 13a). Positions from flows and fronts with black text and arrows. White boxes represent low velocities, red boxes represent high velocities events. Chilean Trench (CHTr). The days with the highest correlations from EOF 1, 2 and 3 are shown as green, yellow and black lines, respectively.

and contourite drift are located at the foot of the continental slope southeast of the SFZ (Figures 16a and 16b). Southwest of the SFZ no contourites have been found at the foot of the slope and this area is characterized by the presence of the SSTr. In contrast, north of the trench large contourite drift with moats around circular topographic highs are found at the seafloor (Figures 16a and 16e). Similar moats around circular topographic obstacles are found in the central SFZ (Figure 17b). Such moats are typically around 250–300 m deep and 8–14 km wide. Moats can be also found along elongated isolated topographic highs, such as in the WDPZ_N (Figures 17a and 17b). In this area, the sub-bottom profile shows the typical morphology and internal structure of a moat, with reflections dipping from the drift side toward the moat and with a decrease in sediment thickness toward the slope (Figure 17b).

In the SFZ_C and in the WDPZ_N, the seafloor topography is very irregular and is dominated by abundant topographic highs. The steep gradients related to this rough topography favors mass wasting processes. Abrupt truncations on the sediment reflections indicate the presence of scars of submarine landslides (Figure 17e), and chaotic and transparent reflections are indicative of mass transport deposits (Figures 17c and 17e). The topographic highs in these areas often present continuous reflections on their top. The sediment thickness tends to decrease toward the sides of the highs and their flanks often present truncations (Figures 17c and 17d).

Grain size analyses of surface sediments indicate that mean sortable silt values are the highest on the top of the topographic highs, with values of around 33 μm east of the central SFZ (Figure 17b). The southern SFZ presents the largest contourite drifts of the study area, which are also characterized by comparatively lower sortable silt values that oscillate between 20 and 23 μm (Figure 16a). In the WDPZ_N area, mean sortable silt values are high at the sample near the moat (32.5 μm) and lower on the top of the topographic high (24.4 μm) (Figure 17a).

4. Discussion and Conclusions

The present study explores the bottom current dynamics of the Antarctic Circumpolar Current (ACC) in the Drake Passage (DP), the interaction of bottom currents with the topography and their role in sedimentation. The regional variability of ACC dynamics near the seafloor was investigated using results from the GLORYS12 reanalysis obtained during 27 years. The current dynamics explained by the data from the GLORYS12 reanalysis are consistent with in situ data as shown already from the validation done by Artana et al. (2021a). The GLORYS 12 reanalysis is considered a barotropic model and the baroclinic component is not as well represented (Artana et al., 2021a, 2021b). The velocity field was investigated in Ferrari et al. (2012) and was found to be similar to the one described by Inoue (1985) with a dominance of the barotropic and first baroclinic modes. Koenig et al. (2014) have shown that the barotropic component is important where velocities are weak, and the baroclinic

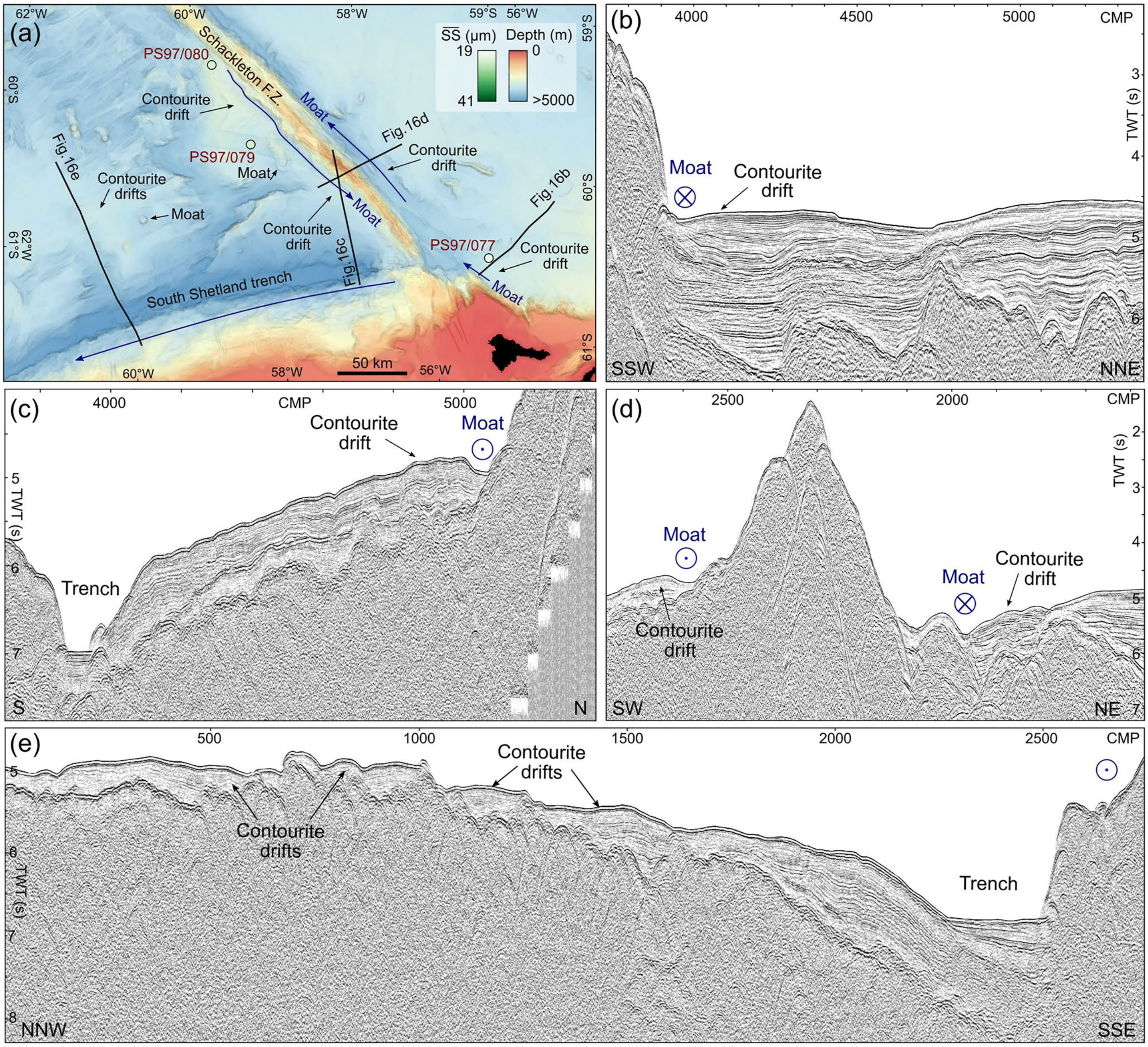

Figure 16. (a) Bathymetric map at the southern region of the Shackleton fracture zone (IBCSO_v2 and multibeam bathymetry from the cruise PS97) showing the location of current-related sedimentary features and mean sortable silt ($\overline{SS}$) of surface sediments (from Wu et al., 2019b). (b)-(e) Seismic reflection profiles showing the presence of moats and contourite drifts. (b) SA500-003, (c) TH88-03B, (d) IT90AP-IT89AW42, (e) TH88-05.

component is more important where upper layer velocities are strong, at frontal locations. In terms of interannual variability, Sallée et al. (2008) investigated the role of the Southern Annular Mode (SAM) and the ENSO index (Niño 3.4) and found that both atmospheric forcings produce a substantial oceanic response, but in different spectral windows. Koenig et al. (2016) found that the total transport of the ACC at the DP is correlated with SAM and ENSO. Koenig et al. (2016) and later Artana et al. (2021a) did not find any systematic relationship, at low frequency, between climate indices SAM and ENSO and DP transport variability, but they reported that the respective impacts are intermittent and epoch-dependent. There is still a need for studying the variability of bottom currents and its response to atmospheric forcing.

In situ hydrographic and sedimentary data from the PS97 Polarstern cruise were considered. We have analyzed the bottom current dynamics of four regions in the DP covering the influence of topographic features, ACC fronts, and sedimentary characteristics. We summarize next the major results and delineate the corresponding conclusions as follows.

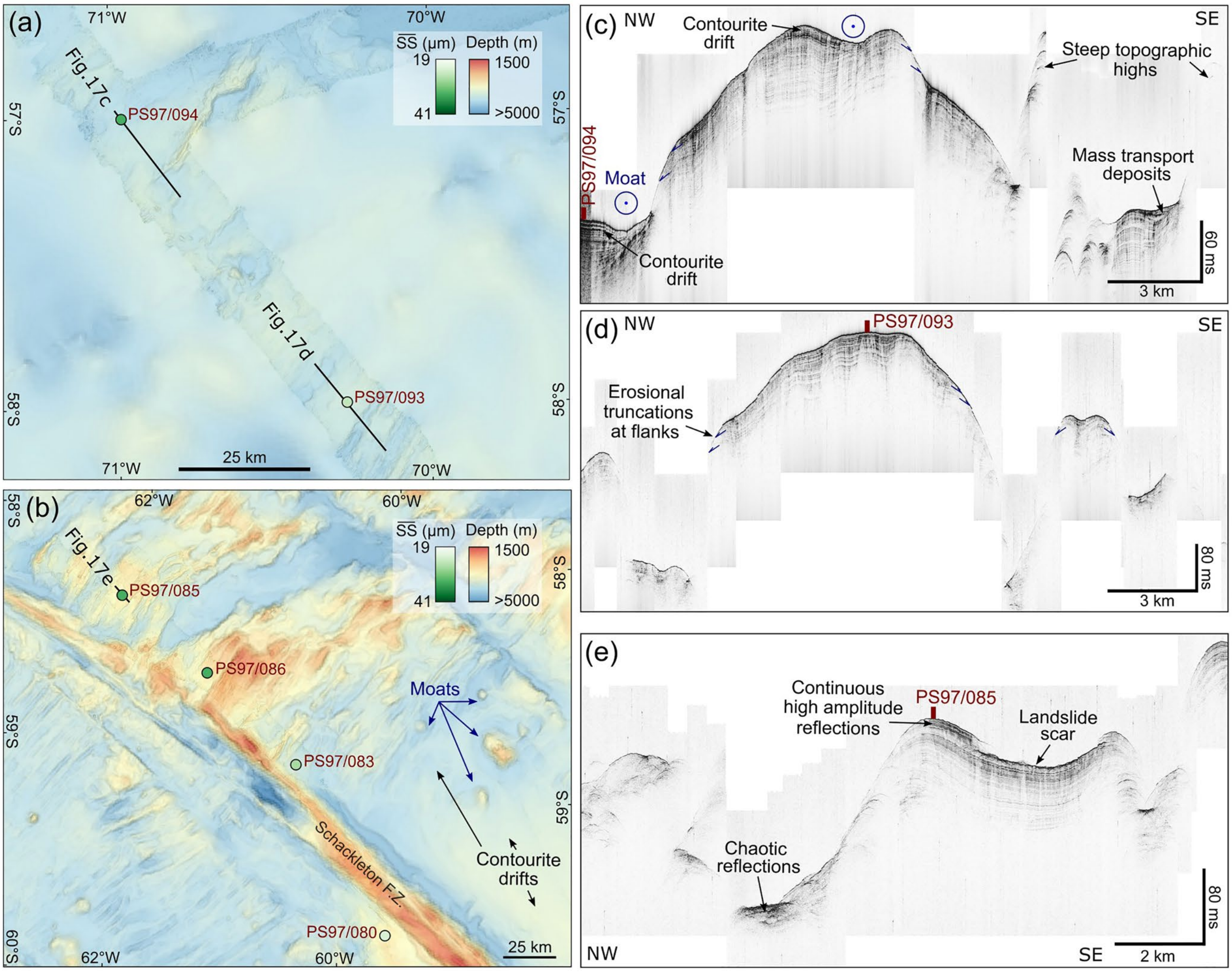

Figure 17. Bathymetric maps and mean sortable silt ($\overline{SS}$) of surface sediments (from Wu et al., 2019b) for the northern region of the West Drake Passage zone (a) and the center region of the Shackleton fracture zone (b) (IBCSO_v2 and multibeam bathymetry from the cruise PS97), showing the irregular and rough topography that characterizes these areas. (c–e) PARASOUND profiles showing current dominated sedimentation and erosion. The red lines and dots indicate the position of sediment cores.

4.1. Shackleton Fracture Zone

The complex topography of the DP (Figure 18) strongly controls the bottom dynamics and therefore, different areas present distinct circulation patterns and variability and are discussed here separately. The zone delimited by the Hero Fracture Zone (HFZ), the Phoenix Antarctic Ridge (PAR), the Shackleton Fracture Zone (SFZ) and the South Shetland Trench (SSTr) can be defined as a region of weak currents and dominated by relatively fine-grained deposits, as indicated by the lowest mean Sortable Silt ($\overline{SS}$) values of the study area (Figures 4, 16, and 18). The reason for these characteristics is that the SACCF avoids the HFZ by heading south (Figure 3) and then when it reaches the SFZ, it tilts north to cross the fracture, or south to pass through the Shackleton Gap (SG) as Provost et al. (2011) and Ferrari et al. (2013) demonstrated. The Polar Front (PF) also avoids this region and deflects north from the HFZ, crossing the SFZ in the intersection with the West Scotia Ridge (WSR) (Orsi et., 1995; Park et al., 2019). This avoidance from these 2 fronts makes this basin less energetic compared to the others in the DP (Figure 3b). The Empirical Orthogonal Function (EOF) analyses for this region (Figures 5a and 5c) show that most of the variability in the flow comes through the SG and the gyre in the Ona Basin (OB), leaving the region located west of the SFZ as the one with lowest variability. The third mode (Figure 5e) shows a different pattern where there is a block in the SG. It is therefore possible to assume that the sediment contribution

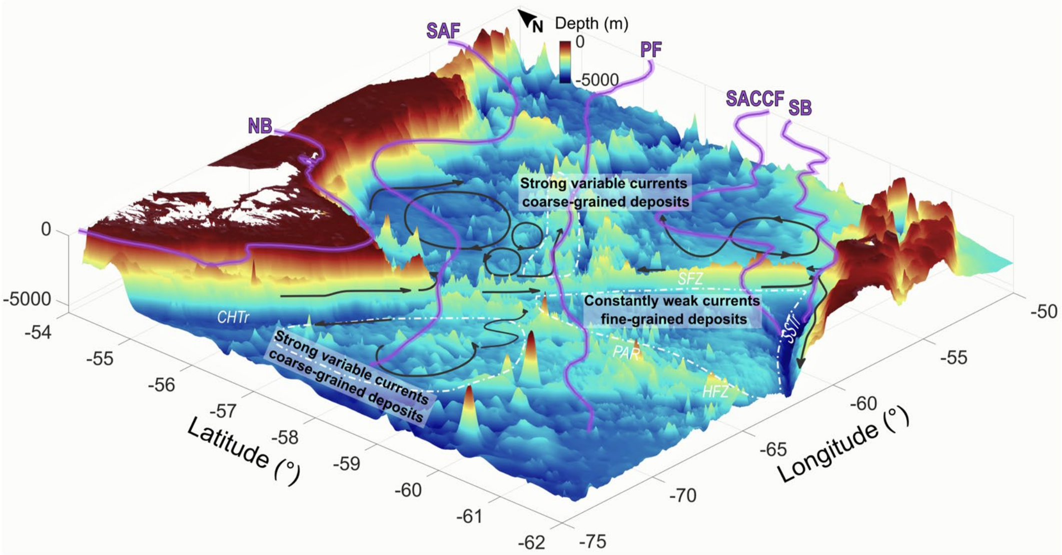

Figure 18. Bathymetric 3D map from Drake Passage (IBCSO_v2) with a schematic representation of circulation near the seafloor in black arrows. The fronts from the Antarctic Circumpolar Current derived from satellite altimetry (Park et al., 2019), and Park and Durand (2019) are represented with purple solid lines. From North to South: NB = North Boundary, SAF = Sub Antarctic Front, PF = Polar Front, SACCF = Southern Antarctic Circumpolar Current Front; SB = Southern Boundary. Shackleton Fracture zone (SFZ); Phoenix Antarctic Ridge (PAR); Hero Fracture Zone (HFZ); South Shetland Trench (SSTr); Chilean Trench (CHTr).

to the SSTr does not only come from the OB and the pre-Weddell Sea, but also from the north-western region of the DP. The anticyclonic gyre in the OB, also observed by Barré et al. (2011), shows a cyclonic phase on the day of the highest correlation for the third mode (Figures 5e and 5f). This eddy has a lifetime of around 15 weeks (Barré et al., 2011). Mesoscale variability in the DP is considered between 40 hr and 90 days (Nowlin et., 1985; Ferrari et al., 2014). In total, 83% of the eddies in the DP are concentrated in the bottom layers and they are trapped by bottom topography (Lin et al., 2023). The third mode should be subject of future investigation. Several sedimentary structures related to bottom currents, such as contourite drifts and moats, have been identified in this area (Figure 16; Maldonado et al., 2003, 2005; Martos et al., 2013; López-Quirós et al., 2020). These features are associated with topographic structures, such as ridges and seamounts and probably form due to the acceleration of bottom currents along these steep slopes (Figure 16). The largest erosional features and widest moats in the study area have been observed east of the SFZ (Figure 16), where bottom currents are fast on average (up to 0.40 m/s) and present relatively high bottom EKE (0.0461 m^2/s^2). In our results, the region located SW of the SFZ presents low values of eddy kinetic energy (EKE) and mean velocity, which correspond to favorable conditions for sedimentation, in agreement with the observed widespread contourite drifts (Figure 16). Thran et al. (2018) argued that contourites are commonly found in zones with high eddy kinetic energy at a global scale when compared to other zones of the ocean floor. However, in this study we show that when bottom-current intensity and variability is analyzed more in detail in zones of contourite depositional systems, it can be observed that muddy contourite drifts are mainly found in zones of relatively low energy, where mean current velocity and EKE are low, as also observed in other areas such as in the Mediterranean Sea and the Mozambique Channel (Miramontes et al., 2019, 2021).

4.2. West Scotia Ridge Confluence

The confluence of the SFZ and the WSR (Figure 7) presents a complex bottom variability in the currents and topography (Figure 18). Ferrari et al. (2012) showed that the PF branches flow in meanders due to the seamounts of the WSR. In our study, we also observe meanders in the bottom currents and high EKE north of the WSR. Surface sediments present high $\overline{SS}$ values in agreement with strong modeled bottom currents in the YB (Figures 17 and 18). Moats and contourites can be found south of the WSR where the flow that came parallel to the SFZ deflects to the NNE. The variability of these zone is dominated by the dynamics in the YB and the confluence of the PF the WSR and the SFZ. PF branches can shift their position (Barré et al., 2011) in this study we observe temporal variability that could be related to them.

The SFZ and the WSR confluence zone are the only ones in the study area where the presence of AABW has been measured (Figures 2a, 2b, and 2d). This is related to the strong effect of the SFZ, which acts as a topographical barrier to westward-flowing water. Only certain gaps over the ridge can allow the East-West over-flow.

4.3. West Drake Passage

The western-most region in this study is the WDPZ, which has been less investigated in previous works. This region is crossed by the NB and SAF from the ACC. An anticyclonic gyre that has not been described before was examined (Figure 10). It was suggested by Park et al. (2019) that the topographic steering is the major dynamic factor controlling the magnitude and direction of the ACC in the chock points regions. This gyre shows the influence of the SAF and topography in steering the bottom current at water depths below 3,000 m. The spatial structure of this first mode of EOF (30%) (Figure 11a) is related to the topographic structures presented in this region. The second mode (10%) (Figure 11c) could be related to the influence of the SAF in the surface or with climate modes of variability. Further studies would be necessary to better understand the genesis and dynamic of this gyre. The third mode (7%) (Figure 11e) shows that when the gyre is disturbed, the center, previously at low velocities, could now have currents that can erode the seafloor or transport sediments around it. Several sedimentary structures associated with bottom currents have been identified in this area. These include contourite drifts and moats (Figure 17).

4.4. Final Considerations

The formation of contourite depositional systems is commonly attributed to relatively constant or persistent bottom currents (Rebesco et al., 2014; and references therein). But in our study, we found events that completely differ from the main flow pattern, as seen in the EOF analysis, and that generate new bottom-current patterns, which could also have an important influence in sedimentation. Moreover, another factor to consider is that mixing in the DP is intense and widespread, even above the complex seafloor topography (Barré et al., 2008; Naveira Garabato et al., 2004, 2007).

As mentioned above, the DP is one of the choke points in the SO within which the ACC flows. The others, the Southwest Indian Ridge, the Kerguelen Plateau, the sector south of the Tasman Sea and the Udinese fracture zone/Eltanin fracture zone in the central South Pacific, could also be explored in the interplay between bottom current dynamics and sedimentary processes. The difficulty of reaching such remote locations to carry out specific and long-term measurement programs, makes satellite information and reanalysis data extra valuable to explore areas where in situ data are sparse or absent.

The variability presented in the three modes of EOF described in this work opens a new insight into the oceanographic processes that control sedimentation in deep-water environments. The mean bottom current field may hide other less frequent and different pattern events that could help explain the sedimentation/erosion processes observed in these complex areas. The identification of contourite features provides the key for decoding past water-mass circulation and the identification of major palaeoceanographic events (Pérez et al., 2015, 2021), this statement opens the way to continue doing interdisciplinary works to understand past and future climate.

To conclude, we underline that.

1. The local topography can significantly affect the hydrodynamic processes near the seafloor, showing a different pattern and disconnection from the dynamics in the sea surface. For instance, the gyre located in the West Drake Passage Zone is constrained by topographic highs but does not seem to be directly affected by the surface front.
2. At Shackleton Gap, the dynamics of the bottom current show that the flow from the Ona Basin is not always constant. Blockages and interruptions can occur. No AABW was found at stations west of the Shackleton fracture zone.
3. The variability in the 27 years of reanalysis can show different patterns in this complex region. The first EOF mode is related with the local topography in each zone. The second and third EOF modes show patterns in the bottom current that differ from the mean field. They could therefore indicate different patterns affecting erosion and sediment deposition.

4. The sedimentary system is strongly controlled by bottom currents in the DP, resulting in the formation of contourites. Moats are related to currents along topographic obstacles that erode and transport the sediments depending on the dynamics that surround them and the largest contourite drifts are found in areas with weak bottom currents and low bottom EKE.
5. Future cruises could be benefitted from this method to evaluate possible locations for coring extraction regarding the bottom current dynamics.

Data Availability Statement

The GLORYS12 reanalysis is available at the Copernicus Marine Environment Monitoring Service (CMEMS; http://marine.copernicus.eu/) product is: https://doi.org/10.48670/moi-00021. The seismic reflection data used in this study were obtained from the Antarctic Seismic Data Library System for Cooperative Research and accessed through the GeoMapApp (http://www.geomapapp.org). The seismic data are available at the Antarctic Seismic Data Library System (SDLS) (https://sdls.ogs.trieste.it). The fronts from the Antarctic Circumpolar Current can be download from (https://doi.org/10.17882/59800). The data collected during the PS97 cruise can be accessed in PANGAEA (https://www.pangaea.de/): PARASOUND profiles (Kuhn, 2016, https://doi.org/10.1594/PANGAEA.864950), multibeam bathymetry (Dorschel & Jensen, 2016, https://doi.org/10.1594/PANGAEA.864807), and CTD measurements (Lamy & Rohardt, 2016, https://doi.org/10.1594/PANGAEA.862944). Grain size data can be also accessed in PANGAEA (Wu et al., 2019a, https://doi.pangaea.de/10.1594/PANGAEA.907140). Also from PANGAEA can be download the International Bathymetric Chart of the Southern Ocean Version 2 (IBCSO v2) (Dorschel et al., 2022, https://doi.org/10.1038/s41597-022-01366-7). Figures and analysis of the GLORYS12 reanalysis were made with MATLAB version: 9.14.0 (R2023a), The MathWorks Inc. 2023, with the package M_Map version 1.4 m (Pawlowicz, 2020). Also, QGIS version 3.28.7 (QGIS Development Team, 2023) was used for bathymetric maps, the IHS Kingdom Software 2019 was used to visualize PARASOUND sub-bottom profiles, Ocean Data View was used for hydrographic figures Schlitzer, 2021).

Acknowledgments

We wish to thank the captain, crew, and scientific party of R/V Polarstern for a successful PS97 cruise. G. Kreps was supported by a fellowship from Deutscher Akademischer Austauschdients (DAAD) under the founding program Research Grants—Bi-nationally Supervised Doctoral Degrees/Cotutelle (57552338). We are grateful to Dr. Catalina Gebhardt for providing the PARADOUND data from the PS97 cruise. Bathymetry data with courtesy of the Alfred Wegener Institute, Helmholtz Centre for Polar and Marine Research. This study has been conducted using E.U. Copernicus Marine Service Information, https://doi.org/10.48670/moi-00021. We thank F. Javier Hernández-Molina and two anonymous reviewers for their constructive comments that helped us improve the manuscript. Open Access funding enabled and organized by Projekt DEAL.

References

Artana, C., Ferrari, R., Bricaud, C., Lellouche, J.-M., Garric, G., Sennéchael, N., et al. (2021a). Twenty-five years of Mercator ocean reanalysis GLORYS12 at Drake Passage: Velocity assessment and total volume transport. *Advances in Space Research*, *68*(2), 447–466. https://doi.org/10.1016/j.asr.2019.11.033

Artana, C., Lellouche, J. M., Park, Y.-H., Garric, G., Koenig, Z., Sennéchael, N., et al. (2018a). Fronts of the Malvinas current system: Surface and subsurface expressions revealed by satellite altimetry, Argo floats, and Mercator operational model output. *Journal of Geophysical Research: Oceans*, *123*(8), 5261–5285. https://doi.org/10.1029/2018JC013887

Artana, C., Lellouche, J.-M., Sennéchael, N., & Provost, C. (2018b). The open-ocean side of the Malvinas Current in Argo float data and 25 years of reanalyses from Mercator operational system. *Journal of Geophysical Research: Oceans*, *123*(11), 8489–8507. https://doi.org/10.1029/2018JC014528

Artana, C., Provost, C., Poli, L., Ferrari, R., & Lellouche, J.-M. (2021b). Revisiting the Malvinas Current upper circulation and water masses using a high-resolution ocean reanalysis. *Journal of Geophysical Research: Oceans*, *126*(6), e2021JC017271. https://doi.org/10.1029/2021JC017271

Barré, N., Provost, C., Renault, A., & Sennéchael, N. (2011). Fronts, meanders and eddies in Drake Passage during the ANT-XXIII/3 cruise in January February 2006: A satellite perspective. *Deep-Sea Research, Part II*, *58*(25–26), 2533–2554. https://doi.org/10.1016/j.dsr2.2011.01.003

Barré, N., Provost, C., Sennéchael, N., & Lee, J. H. (2008). Circulation in the Ona Basin, southern Drake Passage. *Journal of Geophysical Research*, *113*(C4), C04033. https://doi.org/10.1029/2007JC004549

Bohoyo, F., Larter, R. D., Galindo-Zaldívar, J., Leat, P. T., Maldonado, A., Tate, A. J., et al. (2019). Morphological and geological features of Drake Passage, Antarctica, from a new digital bathymetric model. *Journal of Maps*, *15*(2), 49–59. https://doi.org/10.1080/17445647.2018.1543618

Cabanes, C., Grouazel, A., von Schuckmann, K., Hamon, M., Turpin, V., Coatanoan, C., et al. (2013). The CORA dataset: Validation and diagnostics of in-situ ocean temperature and salinity measurements. *Ocean Science*, *9*(1), 1–18. https://doi.org/10.5194/os-9-1-2013

Cattell, R. B. (1966). The scree test for the number of factors. *Multivariate Behavioral Research*, *1*(2), 245–276. https://doi.org/10.1207/s15327906mbr0102_10

Chelton, D. B., Schlax, M. G., Witter, D. L., & Richman, J. G. (1990). Geosat altimeter observations of the surface circulation of the Southern Ocean. *Journal of Geophysical Research*, *95*(C10), 17877–17903. https://doi.org/10.1029/jc095ic10p17877

Copernicus Marine Service (2022). Global ocean physics reanalysis [Dataset]. https://doi.org/10.48670/moi-00021

Deacon, G. E. R. (1937). The hydrology of the Southern Ocean. *Discovery Reports*, *15*, 3–122.

Dong, S., Sprintall, J., & Gille, S. T. (2006). Location of the polar front from AMSR-E satellite sea surface temperature measurements. *Journal of Physical Oceanography*, *36*(11), 2075–2089. https://doi.org/10.1175/JPO2973.1

Dorschel, B., Hehemann, L., Viquerat, S., Warnke, F., Dreutter, S., Tenberge, Y. S., et al. (2022). The International bathymetric chart of the Southern Ocean Version 2 [Dataset]. Scientific Data, *9*, 275. https://doi.org/10.1038/s41597-022-01366-7

Dorschel, B., & Jensen, L. (2016). Swath sonar bathymetry during POLARSTERN cruise PS97 (ANT-XXXI/3) with links to multibeam raw data files [Dataset]. Alfred Wegener Institute, Helmholtz Centre for Polar and Marine Research, Bremerhaven, PANGAEA. https://doi.org/10.1594/PANGAEA.864807

Eagles, G., & Jokat, W. (2014). Tectonic reconstructions for paleobathymetry in Drake Passage. *Tectonophysics*, *611*, 28–50. https://doi.org/10.1016/j.tecto.2013.11.021

Faugères, J. C., Stow, D. A., Imbert, P., & Viana, A. (1999). Seismic features diagnostic of contourite drifts. *Marine Geology*, *162*(1), 1–38. https://doi.org/10.1016/s0025-3227(99)00068-7

Faugères, J. C., & Stow, D. A. V. (2008). Contourite drifts: Nature, evolution and controls. *Developments in sedimentology*, *60*, 257–288.

Ferrari, R., Provost, C., Barré, N., Sennéchael, N., & Lee, J. H. (2013). Circulation in Drake Passage revisited using new current time series and satellite altimetry: 2. The Ona Basin. *Journal of Geophysical Research: Oceans*, *118*(1), 147–165. https://doi.org/10.1029/2012JC008193

Ferrari, R., Provost, C., Park, Y.-H., Sennéchael, N., Koenig, Z., Sekma, H., et al. (2014). Heat fluxes across the Antarctic circumpolar current in Drake Passage: Mean flow and eddy contributions. *Journal of Geophysical Research: Oceans*, *119*(9), 6381–6402. https://doi.org/10.1002/2014jc010201

Ferrari, R., Provost, C., Renault, A., Sennéchael, N., Barré, N., Park, Y.-H., & Lee, J. H. (2012). Circulation in Drake Passage revisited using new current time-series and satellite altimetry. Part I: The Yaghan Basin. *Journal of Geophysical Research: Oceans*, *117*(C12). https://doi.org/10.1029/2012JC008264

Gill, A. E., Green, J. S., & Simmons, A. J. (1974). Energy partition in the large-scale ocean circulation and the production of mid-ocean eddies. *Deep-Sea Research*, *21*(7), 499–528. https://doi.org/10.1016/0011-7471(74)90010-2

Grant, J. A., & Schreiber, R. (1990). Modern swathe sounding and sub-bottom profiling technology for research applications: The Atlas hydrosweep and parasound systems. *Marine geological surveying and sampling*, *12*(1–2), 9–19. https://doi.org/10.1007/bf00310559

Greene, C. A., Thirumalai, K., Kearney, K. A., Delgado, J. M., Schwanghart, W., Wolfenbarger, N. S., et al. (2019). The climate data toolbox for MATLAB. *Geochemistry, Geophysics, Geosystems*, *20*(7), 3774–3781. https://doi.org/10.1029/2019GC008392

Inoue, M. (1985). Modal decomposition of the low-frequency currents and baroclinic instability at Drake Passage. *Journal of physical oceanography*, *15*(9), 1157–1181.

Jackett, D. R., & MacDougall, T. J. (1997). A neutral density variable for the world's oceans. *Journal of Physical Oceanography*, *27*(2), 237–263. https://doi.org/10.1175/1520-0485(1997)027<0237:andvft>2.0.co;2

Jacobs, S. (2004). Bottom water production and its links with the thermohaline circulation. *Antarctic Science*, *16*(4), 427–437. https://doi.org/10.1017/S095410200400224X

Khatiwala, S., Primeau, F., & Hall, T. (2009). Reconstruction of the history of anthropogenic CO+ concentrations in the ocean. *Nature*, *462*(7271), 346–349. https://doi.org/10.1038/nature08526

Klinck, J. M. (1985). EOF analysis of central Drake Passage currents from DRAKE 79. *Journal of Physical Oceanography*, *15*(3), 288–298. https://doi.org/10.1175/1520-0485(1985)015<0288:EAOCDP>2.0.CO;2

Klinck, J. M., & Hofmann, E. E. (1986). Deep-flow variability at Drake Passage. *Journal of Physical Oceanography*, *16*(7), 1281–1292. https://doi.org/10.1175/1520-0485(1986)016<1281:dfvadp>2.0.co;2

Koenig, Z., Provost, C., Ferrari, R., Sennéchael, N., & Rio, M. H. (2014). Volume transport of the Antarctic circumpolar current: Production and validation of a 20 year long time series obtained from in situ and satellite observations. *Journal of Geophysical Research: Oceans*, *119*(8), 5407–5433. https://doi.org/10.1002/2014jc009966

Koenig, Z., Provost, C., Park, Y. H., Ferrari, R., & Sennéchael, N. (2016). Anatomy of the Antarctic circumpolar current volume transports through Drake passage. *Journal of Geophysical Research: Oceans*, *121*(4), 2572–2595. https://doi.org/10.1002/2015jc011436

Kuhn, G. (2016). Profile of sediment echo sounding during POLARSTERN cruise PS97 (ANT-XXXI/3) with links to ParaSound data files [Dataset]. Alfred Wegener Institute, Helmholtz Centre for Polar and Marine Research, Bremerhaven, PANGAEA. https://doi.org/10.1594/PANGAEA.864950

Lamy, F. (2016). The expedition PS97 of the research vessel POLARSTERN to the Drake passage in 2016. *Berichte zur Polar-und Meeresforschung Reports on polar and marine research*, *701*. https://doi.org/10.2312/BzPM_0701_2016

Lamy, F., Arz, H. W., Kilian, R., Lange, C. B., Lembke-Jene, L., Wengler, M., et al. (2015). Glacial reduction and millennial-scale variations in Drake Passage throughflow. *Proceedings of the National Academy of Sciences*, *112*(44), 13496–13501. https://doi.org/10.1073/pnas.1509203112

Lamy, F., & Rohardt, G. (2016). CTD raw data files from POLARSTERN cruise PS97, link to tar file [Dataset]. Alfred Wegener Institute, Helmholtz Centre for Polar and Marine Research, Bremerhaven, PANGAEA. https://doi.org/10.1594/PANGAEA.862944

Ledbetter, M., & Johnson, D. A. T. (1976). Increased transport of Antarctic bottom water in the Vema channel during the last ice age. Science, *194*(4267), 837–839. https://doi.org/10.1126/science.194.4267.837

Lellouche, J.-M., Greiner, E., Le Galloudec, O., Garric, G., Regnier, C., Drevillon, M., et al. (2018). Recent updates on the Copernicus Marine Service global ocean monitoring and forecasting real-time 1/12 high resolution system. *Ocean Science*, *14*, 1093–1126. https://doi.org/10.5194/os-2018-15

Lellouche, J.-M., Le Galloudec, O., Drévillon, M., Régnier, C., Greiner, E., Garric, G., et al. (2013). Evaluation of real time and future global monitoring and forecasting systems at Mercator Ocean. *Ocean Science Discussions*, *9*, 1123–1185. https://doi.org/10.5194/osd-9-1123-2012

Lin, X., Zhao, H., Liu, Y., Han, G., Zhang, H., & Liao, X. (2023). Ocean eddies in the Drake Passage: Decoding their three-dimensional structure and evolution. *Remote Sensing*, *15*(9), 2462. https://doi.org/10.3390/rs15092462

Livermore, R., Eagles, G., Morris, P., & Maldonado, A. (2004). Shackleton fracture zone: No barrier to early circumpolar ocean circulation. *Geology*, *32*(9), 797–800. https://doi.org/10.1130/g20537.1

Lobo, F. J., López-Quirós, A., Hernández-Molina, F. J., Pérez, L. F., García, M., Evangelinos, D., et al. (2021). Recent morpho-sedimentary processes in Dove Basin, southern Scotia Sea, Antarctica: A basin-scale case of interaction between bottom currents and mass movements. *Marine Geology*, *441*, 106598. https://doi.org/10.1016/j.margeo.2021.106598

López-Quirós, A., Lobo, F. J., Escutia, C., García, M., Hernández-Molina, F. J., Pérez, L. F., et al. (2020). Geomorphology of Ona Basin, southwestern Scotia Sea (Antarctica): Decoding the spatial variability of bottom-current pathways. *Marine Geology*, *422*, 106113. https://doi.org/10.1016/j.margeo.2020.106113

Madec, G., & the NEMO team. (2008). *NEMO ocean engine* (pp. 1288–1619). Note du Pole de modelisation, Institut Pierre-Simon Laplace (IPSL).

Maldonado, A., Barnolas, A., Bohoyo, F., Escutia, C., Galindo-Zaldívar, J., Hernández-Molina, F. J., et al. (2005). Miocene to recent contourite drifts development in the northern Weddell Sea (Antarctica). In F. Florindo, D. M. Harwood, & G. S. Wilson (Eds.), *Long-term changes in Southern high-latitude ice sheets and climate: The Cenozoic history*, (Vol. 45, pp. 99–129). Global and Planetary Change. https://doi.org/10.1016/j.gloplacha.2004.09.013

Maldonado, A., Barnolas, A., Bohoyo, F., Galindo-Zaldívar, J., Hernández-Molina, F. J., Lobo, F., et al. (2003). Contourite deposits in the central Scotia Sea: The importance of the Antarctic Circumpolar Current and the Weddell Gyre flows. *Paleogeography, Paleoclimatology, Paleoecology*, *198*(1–2), 187–221. https://doi.org/10.1016/S0031-0182(03)00401-2

Maldonado, A., Bohoyo, F., Galindo-Zaldívar, J., Hernández-Molina, F. J., Lobo, F. J., Lodolo, E., et al. (2014). A model of oceanic development by ridge jumping: Opening of the Scotia Sea. *Global and Planetary Change*, *123*, 152–173. https://doi.org/10.1016/j.gloplacha.2014.06.010

Marshall, J., & Speer, K. (2012). Closure of the meridional overturning circulation through Southern Ocean upwelling. *Nature Geoscience*, *5*(3), 171–180. https://doi.org/10.1038/ngeo1391

Martos, Y., Maldonado, A., Lobo, F. J., Hernández-Molina, F. J., & Pérez, L. F. (2013). Tectonics and palaeoceanographic evolution recorded by contourite features in southern Drake Passage (Antarctica). *Marine Geology*, *343*, 73–91. https://doi.org/10.1016/j.margeo.2013.06.015

McCave, I. N., & Hall, I. R. (2006). Size sorting in marine muds: Processes, pitfalls, and prospects for paleoflow-speed proxies. *Geochemistry, Geophysics, Geosystems*, *7*(10). https://doi.org/10.1029/2006gc001284

McCave, I. N., Manighetti, B., & Robinson, S. G. (1995). Sortable silt and fine sediment size/composition slicing: Parameters for palaeocurrent speed and palaeoceanography. *Paleoceanography*, *10*(3), 593–610. https://doi.org/10.1029/94PA03039

McCave, I. N., & Swift, S. A. (1976). A physical model for the rate of deposition of fine-grained sediments in the deep sea. *GSA Bulletin*, *87*(4), 541–546. https://doi.org/10.1130/0016-7606(1976)87<541:APMFTR>2.0.CO;2

McCave, I. N., Thornalley, D. J. R., & Hall, I. R. (2017). Relation of sortable silt grain-size to deep-sea current speeds: Calibration of the 'Mud Current Meter'. *Deep Sea Research Part I: Oceanographic Research Papers*, *127*, 1–12. https://doi.org/10.1016/j.dsr.2017.07.003

Meredith, M. P., Woodworth, P. L., Chereskin, T. K., Marshall, D. P., Allison, L. C., Bigg, G. R., et al. (2011). Sustained monitoring of the Southern Ocean at Drake Passage: Past achievements and future priorities. *Reviews of Geophysics*, *49*(4), RG4005. https://doi.org/10.1029/2010RG000348

Miramontes, E., Garreau, P., Caillaud, M., Jouet, G., Pellen, R., Hernández-Molina, F. J., et al. (2019). Contourite distribution and bottom currents in the NW Mediterranean Sea: Coupling seafloor geomorphology and hydrodynamic modelling. *Geomorphology*, *333*, 43–60. https://doi.org/10.1016/j.geomorph.2019.02.030

Miramontes, E., Thiéblemont, A., Babonneau, N., Penven, P., Raisson, F., Droz, L., et al. (2021). Contourite and mixed turbidite-contourite systems in the Mozambique Channel (SW Indian Ocean): Link between geometry, sediment characteristics and modelled bottom currents. *Marine Geology*, *437*, 106502. https://doi.org/10.1016/j.margeo.2021.106502

Moore, J. K., Abbott, M. R., & Richman, J. G. (1999). Location and dynamics of the Antarctic Polar Front from satellite sea surface temperature data. *Journal of Geophysical Research*, *104*(C2), 3059–3073. https://doi.org/10.1029/1998jc900032

Naveira Garabato, A. C., Heywood, K. J., & Stevens, D. P. (2002). Modification and pathways of Southern Ocean deep waters in the Scotia Sea. *Deep-Sea Research I*, *49*(4), 681–705. https://doi.org/10.1016/s0967-0637(01)00071-1

Naveira Garabato, A. C., Polzin, K. L., King, B. A., Heywood, K. J., & Visbeck, M. (2004). Widespread intense turbulent mixing in the Southern Ocean. *Science*, *303*(5655), 210–213. https://doi.org/10.1126/science.1090929

Naveira Garabato, A. C., Stevens, D. P., Watson, A. J., & Roether, W. (2007). Short-circuiting of the overturning circulation in the Antarctic Circumpolar Current. *Nature*, *447*(7141), 194–197. https://doi.org/10.1038/nature05832

Nielsen, T. A. P. M., Knutz, P. C., & Kuijpers, A. (2008). Seismic expression of contourite depositional systems. *Developments in Sedimentology*, *60*, 301–321.

Nowlin, W. D., Jr., Worley, S. J., & Whitworth, T., III. (1985). Methods for making point estimates of eddy heat flux as applied to the Antarctic Circumpolar Current. *Journal of Geophysical Research*, *90*(C2), 3305–3324. https://doi.org/10.1029/jc090ic02p03305

Orsi, A. H., Johnson, G. C., & Bullister, J. L. (1999). Circulation, mixing, and production of Antarctic bottom water. *Progress in Oceanography*, *43*(1), 55–109. https://doi.org/10.1016/s0079-6611(99)00004-x

Orsi, A. H., Whitworth, T., III, & Nowlin, W. D., Jr. (1995). On the meridional extent and fronts of the Antarctic Circumpolar Current. *Deep-Sea Research, Part A: Oceanographic Research Papers I*, *42*(5), 641–673. https://doi.org/10.1016/0967-0637(95)00021-w

Park, Y., Park, T., Kim, T., Lee, S., Hong, C., Lee, J., et al. (2019). Observations of the Antarctic circumpolar current over the Udintsev fracture zone, the narrowest choke point in the Southern Ocean. *Journal of Geophysical Research: Oceans*, *124*(7), 4511–4528. https://doi.org/10.1029/2019JC015024

Park, Y. H., & Durand, I. (2019). Altimetry-drived Antarctic circumpolar current fronts [Dataset]. SEANOE. https://doi.org/10.17882/59800

Pawlowicz, R. (2020). "M_Map: A mapping package for MATLAB", version 1.4m [Software]. Retrieved from www.eoas.ubc.ca/~rich/map.html

Pedlosky, J. (1987). *Geophysical fluid dynamics* (2nd ed.). Springer-Verlag.

Pérez, L. F., Hernández-Molina, F. J., Esteban, F. D., Tassone, A., Piola, A. R., Preu, B., et al. (2015). Erosional and depositional contourite features at the western Scotia Sea - Southern Atlantic Ocean transition: Correlations with regional water masses circulation. *Geo-Marine Letters*, *35*(4), 271–288. https://doi.org/10.1007/s00367-015-0406-6

Pérez, L. F., Martos, Y. M., García, M., Weber, M. E., Raymo, M. E., Williams, T., et al. (2021). Miocene to present oceanographic variability in the Scotia Sea and Antarctic ice sheets dynamics: Insight from revised seismic-stratigraphy following IODP Expedition 382. *Earth and Planetary Science Letters*, *553*, 116657. https://doi.org/10.1016/j.epsl.2020.116657

Provost, C., Renault, A., Barré, N., Sennéchael, N., Garçon, V., Sudre, J., & Huhn, O. (2011). Two repeat crossings of Drake Passage in Austral Summer 2006: Short-term variations and evidence for considerable ventilation of intermediate and deep waters. *Deep Sea Research Part II: Topical Studies in Oceanography*, *58*(25–26), 2555–2571. https://doi.org/10.1016/j.dsr2.2011.06.009

Pujol, M.-I., Faugère, Y., Taburet, G., Dupuy, S., Pelloquin, C., Ablain, M., & Picot, N. (2016). DUACS DT2014: The new multi-mission altimeter data set reprocessed over 20 years. *Ocean Science*, *12*(5), 1067–1090. https://doi.org/10.5194/os-12-1067-2016

QGIS Development Team. (2023). QGIS geographic information system [Software]. Open-Source Geospatial Foundation Project. Retrieved from http://qgis.osgeo.org

Rebesco, M., & Camerlenghi, A. (2008). *Contourites*. Elsevier.

Rebesco, M., Hernández-Molina, F. J., Van Rooij, D., & Wåhlin, A. (2014). Contourites and associated sediments controlled by deep-water circulation processes: State-of-the-art and future considerations. *Marine Geology*, *352*, 111–154. https://doi.org/10.1016/j.margeo.2014.03.011

Rintoul, S. R., & Sokolov, S. (2001). Baroclinic transport variability of the Antarctic Circumpolar Current south of Australia (WOCE repeat section SR3). *Journal of Geophysical Research*, *106*(C2), 2795–2814. https://doi.org/10.1029/2000JC900107

Sallée, J. B., Speer, K., & Morrow, R. (2008). Response of the Antarctic circumpolar current to atmospheric variability. *Journal of Climate*, *21*(12), 3020–3039. https://doi.org/10.1175/2007jcli1702.1

Schlitzer, R. (2021). Ocean data view [Software]. https://odv.awi.de

Sokolov, S., & Rintoul, S. R. (2009). Circumpolar structure and distribution of the Antarctic circumpolar current fronts: 2. Variability and relationship to sea surface height. *Journal of Geophysical Research*, *114*(C11), C11019. https://doi.org/10.1029/2008JC005248

Solodoch, A., Stewart, A. L., Hogg, A. M., Morrison, A. K., Kiss, A. E., Thompson, A. F., et al. (2022). How does Antarctic bottom water cross the Southern Ocean? *Geophysical Research Letters*, *49*(7), e2021GL097211. https://doi.org/10.1029/2021GL097211

Speer, K., Rintoul, S. R., & Sloyan, B. (2000). The diabatic Deacon cell. *Journal of Physical Oceanography*, *30*(12), 3212–3222. https://doi.org/10.1175/1520-0485(2000)030<3212:tddc>2.0.co;2

Sverdrup, H. U. (1933). On vertical circulation in the ocean due to the action of the wind with application to conditions within the Antarctic circumpolar current. *Discovery Reports*, *VII*, 139–170.

Szekeley, T., Gourrion, J., Pouliquen, S., & Reverdin, G. (2016). CORA, coriolis, ocean dataset for reanalysis. *SEANOE*. https://doi.org/10.1029/2008JC05248

The MathWorks Inc. (2023). MATLAB version: 9.14.0 (R2023a) [Software]. The MathWorks Inc. Retrieved from https://www.mathworks.com

Thran, A. C., Dutkiewicz, A., Spence, P., & Müller, R. D. (2018). Controls on the global distribution of contourite drifts: Insights from an eddy-resolving ocean model. *Earth and Planetary Science Letters*, *489*, 228–240. https://doi.org/10.1016/j.epsl.2018.02.044

Toyos, M. H., Lamy, F., Lange, C. B., Lembke-Jene, L., Saavedra-Pellitero, M., Esper, O., & Arz, H. W. (2020). Antarctic circumpolar current dynamics at the pacific entrance to the Drake Passage over the past 1.3 million years. *Paleoceanography and Paleoclimatology*, *35*(7), e2019PA003773. https://doi.org/10.1029/2019pa003773

Valla, D., Piola, A. R., Meinen, C. S., & Campos, E. (2018). Strong mixing and recirculation in the northwestern Argentine Basin. *Journal of Geophysical Research: Oceans*, *123*(7), 4624–4648. https://doi.org/10.1029/2018JC013907

Venaille, A., Vallis, G. K., & Smith, K. S. (2011). Baroclinic turbulence in the ocean: Analysis with primitive equation and quasigeostrophic simulations. *Journal of Physical Oceanography*, *41*(9), 1605–1623. https://doi.org/10.1175/JPO-D-10-05021.1

Well, R., Roether, W., & Stevens, D. P. (2003). An additional deep-water mass in Drake Passage as revealed by 3He data. *Deep-Sea Res. Pt. I*, *50*(50), 1079–1098. https://doi.org/10.1016/S0967-0637(03)00050-5

Wilckens, H., Miramontes, E., Schwenk, T., Artana, C., Zhang, W., Piola, A. R., et al. (2021). The erosive power of the Malvinas Current: Influence of bottom currents on morpho-sedimentary features along the northern Argentine margin (SW Atlantic Ocean). *Marine Geology*, *439*, 106539. https://doi.org/10.1016/j.margeo.2021.106539

Wu, S., Kuhn, G., Diekmann, B., Lembke-Jene, L., Tiedemann, R., Zheng, X., et al. (2019a). Grain size and bulk composition of ocean sediments between South America and the Antarctic Peninsula. PANGAEA [Dataset]. https://doi.org/10.1594/PANGAEA.907140

Wu, S., Kuhn, G., Diekmann, B., Lembke-Jene, L., Tiedemann, R., Zheng, X., et al. (2019b). Surface sediment characteristics related to provenance and ocean circulation in the Drake Passage sector of the Southern Ocean. Deep-Sea Research Part I, *154*. https://doi.org/10.1016/j.dsr.2019.103135

Wu, S., Lembke-Jene, L., Lamy, F., Arz, H. W., Nowaczyk, N., Xiao, W., et al. (2021). Orbital-and millennial-scale Antarctic circumpolar current variability in Drake passage over the past 140,000 years. *Nature Communications*, *12*(1), 1–9. https://doi.org/10.1038/s41467-021-24264-9